Analysis of wrinkled membrane structures using a Plane Stress projection procedure and the Dynamic Relaxation method

H. Le Meitour, G. Rio, H. Laurent, A.S. Lectez, P. Guigue

Analysis of wrinkled membrane structures using a Plane Stress projection procedure and the Dynamic Relaxation method

H. Le Meitour[a], G. Rio[a], H. Laurent[a,*], A. S. Lectez[b], P. Guigue[b]

[a] *Univ. Bretagne Sud, UMR CNRS 6027, IRDL, F-56100 Lorient, France*
[b] *CNES, Centre Spatial de Toulouse, 18 avenue Edouard Belin, F-31401 Toulouse cedex 9, France*

Abstract

Deployable membrane structures such as inflatable stratospheric balloons are known to be sensitive to the occurrence of local instabilities such as wrinkles. The wrinkling phenomenon affects the working performances of the membrane and the occurrence of this phenomenon has to be controlled numerically in order to predict the best means of deployment during the inflation of aerospace balloons. To improve their performances and reliability during flight, the balloons also need to be sized appropriately without the stress field being disturbed by the wrinkles. These instabilities originate numerically from the membrane elements which have a negligible bending stiffness. Several wrinkling models have been presented in the literature in order to solve this problem. However, in most of these models an elastic law and the Green deformation approach have been used for this purpose.

The new model called the PS-DPS model presented here for correcting the effects of wrinkles on membrane structures was implemented in the in-

*Corresponding author
Email address: herve.laurent@univ-ubs.fr (H. Laurent)
URL: http://irdl.fr/ (H. Laurent)

Revised version submitted to International Journal of Solids and Structures October 26, 2020

house finite element software Herezh++. A projection technique based on a Newton-Raphson method is used to control the stress plane and the in-plane contraction. Using the Almansi strain formulation, this model also accounts for the changes in membrane thickness liable to occur during simulations. The problems due to numerical instabilities are overcome by determining the equilibrium with the so-called Dynamic Relaxation method using kinetic damping procedures. Unlike other membrane models of literature, the PS-DPS model can be used with materials showing complex mechanical behaviour of all kinds. Several benchmark problems are analysed with the present wrinkling model and compared with results available in the literature, focusing first on an elastic law and then on a non-linear hyperelastic law. Lastly, the inflation of a square cushion test and that of a Zero Pressure Balloon are simulated with this non-linear law. The results obtained indicate that the PS-DPS model is valid and accurate to take into account the wrinkles in flexible structures with all these linear and non-linear behaviours.
Keywords: Wrinkling model, Membrane structures, Inflated structures, Dynamic Relaxation method, Plane Stress projection procedure, Non-linear behaviour

---

1. Introduction

Inflated stratospheric balloons made of thin plastic film are widely used by the French Space Agency (CNES) for studying atmospheric and astronomic phenomena and testing technological innovations. Due to the large size of these balloons (which measure anything up to 180 m in height) and the flexibility of their polyethylene envelope (which is only a few tens of μm thick), inflation of the stratospheric balloons causes local buckling phenomena, which appears as wrinkling. These buckling processes are due to the fact that these membrane structures, which have been referred to as "without compression", have a negligible bending stiffness. If no compressive stress is induced in the membrane, an out-of-plane displacement of the membrane will occur, resulting in wrinkles.

The number of numerical studies on wrinkled structures such as flexible membranes and fine fabric structures has increased considerably since the 1990s. Jenkins in his 1996 review <1> was the first to not only outline the problem of wrinkling, but also to cover all the aspects of the theory and applications of thin structures that can be defined as membranes. Several reviews <2–9> have been subsequently published on the various finite element methods developed for simulating wrinkling problems. The basic idea was introduced by Wagner <10>, based in particular on Tension-Field (TF) theory, and on the assumption that a membrane has no bending stiffness and cannot resist any compression forces. Many wrinkling models (see for example <6; 11>) have since been developed on these lines for predicting the wrinkling direction and eliminating the in-plane stiffness in the direction perpendicular to the wrinkles.

Thus, the first type of wrinkling model was to modify the deformation gradient tensor to represent TF responses of wrinkled membranes <12; 13>.

By introducing the concept of relaxed energy density, Pipkin <14> defined membrane wrinkling as a problem of energy minimization arising in the case of elastic bodies devoid of bending rigidity. This method inspired several other models <15–17>, and Epstein and Forcinito <18> extended this relaxed energy function model to include anisotropic membranes by introducing the idea of saturated elasticity and by modifying the Green's strain tensor.

The second approach, on which this paper focuses, is based on a local modification of the stress-strain relationship within an element, *i.e.* the constitutive equation is modified in order to eliminate all the compressive stresses <19>. In this case, there exist several possible solutions. One of them consists in modifying the stiffness tensor of elasticity by adding a corrective factor <4; 20–22>. Another one consists in modifying the constants of the material such as the modulus of elasticity and/or the Poisson's ratio <23–26>. Another method consists in post-multiplying the stiffness matrix with a projection matrix that eliminates the compressive stresses <19; 27>. The influence of these various solutions can be seen in the paper by Wang et al. <6>. These previous approaches provide a rigorous mathematical formulation of the wrinkling mechanism and can easily be applied to existing finite element codes for the analysis of membrane structures with wrinkles. However, the exact physical significance of the modified elasticity matrix is somewhat obscure because of the arbitrary choice of projection matrix.

The last approach to modelling wrinkles worth mentioning consists in using thin shell elements that include both membrane and bending contributions and can be used to model the amplitude and wavelength of wrinkles. This method has been adopted in several studies (*e.g.* <3; 28>). Unfortunately, in order to obtain sufficiently realistic results, the mesh size must be sufficiently fine which requires fairly long computational times. Shell el-

ements are naturally more expensive in terms of computational time than membrane elements because a large number of degrees of freedom (rotations) and integration points (through the thickness) is required. During the last few years, however, shell elements devoid rotational degrees of freedom have been developed <29–32> and used to model the shape of wrinkles on isotropic and anisotropic flexible structures <33>. Elements of this kind are the most efficient for modelling the wrinkles phenomena in small structures, but in the case of large structures such as stratospheric balloons, this option does not seem to be the most efficient due to the long computational times induced by the mesh size. In addition, it is worth noting that the wrinkling behaviour (*i.e.* buckling) often depends on the size and type of mesh.

Finding suitable means of modelling wrinkling processes in the design stage is therefore an important challenge for constructing reliable membrane-based space structures <34>. It is of the utmost importance to be able to predict the behaviour of membrane wrinkles, including the direction in which they occur and what stresses are at work in the case of inflated stratospheric balloons <11>. However, most previous studies have focused so far on determining the direction of the wrinkling process and the corresponding stress state in the case of materials with isotropic <7; 14; 35> or anisotropic linear behaviour <12; 17; 18; 22; 36> as well as for linear viscoelastic behaviour <37–40>. However, in the case of materials with non linear behaviour, this subject still requires further investigation <41; 42>, and in the context of stratospheric balloons, it should be noted that thin films show complex behaviour characterized by large irreversible strains and strain rate dependency, and therefore, elasto-visco-plastic behaviour. In this context, the aim of this paper is to present a new simple, accurate method of modelling membrane structures giving the wrinkling directions for all kinds of material behaviours.

This model, which we have called the "Plane Stress-Double Plane Stress" (PS-DPS) model, is based on two approaches. The first approach consists in adjusting the components of the constitutive tensor in the direction of the compressive stress. The principle underlying this method is in fact consistent with other approaches used in <4; 19; 43>, for example, but the Newton-Raphson method of projection used here makes it possible to control the constitutive matrix in the case of materials of all kinds. In this case, the aim is not to simulate the shape of the wrinkles but to account for their occurrence on the equilibrium state of the membrane. Another originality feature of this model is that the thickness of the membrane structure is updated throughout the simulation.

The second approach used in the PS-DPS model overcomes the numerical instabilities that are liable to occur due to the poor convergence of the numerical resolution of the membrane structure. This is can be explained by the fact that the local stiffness of the membrane can vary between large positive values and zero during the iterative process. A Dynamic Relaxation (DR) method (which is also known as the pseudo-Dynamic method) is then introduced to determine the global equilibrium in the analysis of undercon-strained membranes <44; 45>.

These two approaches and the DR method are implemented in the in-house finite element software Herezh++ <46–48>. In the literature, wrinkled membrane models have been classically written based on the initial configuration of the structure using the Green strain tensor <6; 7; 27> whereas the PS-DPS model is written here based on the current configuration of the structure using the Almansi strain measure and the Cauchy stress tensor.

This paper is structured as follows: the numerical methods used to develop the PS-DPS model are presented in Section 2. The distinctive char-

acteristics of the Plane Stress and Double Plane Stress approaches are explained in sections 2.3 and 2.4 respectively. The pseudo-Dynamic process is then described in section 3. To show the accuracy and potential of the present model, several benchmark examples are modelled and analysed in section 4 using isotropic elastic law and compare with results available in the literature. First, structures constrained in their planes are studied. Shear test is first analysed since this is the most widely used test for checking the validity of wrinkling models. In this test, the membrane is fully wrinkled (in either a single direction or all possible directions) in order to check the accuracy of the PS-DPS model. The results of a torsion test in which the membrane shifts locally from a wrinkled to a taut state is then compared with an analytical solution. Next, a square cushion deployment is carried out in order to test the model on a structure resembling that of stratospheric balloon. In this test, comparisons are also made with finite element simulations performed with Abaqus <49> using the "No compression" procedure, in which the elastic behaviour is modified by imposing the appropriate principal stress at zero. To determine the influence of behavioral laws on the results obtained, the inflation of a square cushion test is also simulated using a hyperelastic law with the PS-DPS model in section 4.4. Lastly, in section 5, to show the applicability of the PS-DPS model in a real case of balloon inflation, simulations of the deployment of a Zero Pressure Balloon with both elastic and non linear laws are presented.

2. The PS−DPS model

Before presenting the PS−DPS model, some notations are introduced in order to explain the kinematic hypotheses and tensor notations used. First, let us take a Gauss point M and the associated material frame $\{M, \vec{g}_i\}$ (where

$i = 1 \ldots 3$). The covariant base vectors, which follow the point M as a function of time t, are defined in the tangent membrane plane, using a curvilinear coordinate system θ^{α}, by:

$$\vec{g}_{\alpha}(t) = \frac{\partial \vec{M}_{(t)}}{\partial \theta^{\alpha}} \text{ with } \alpha = 1, 2 \tag{1}$$

In the Herezh++ software, these curvilinear coordinates constituting a set of material coordinates are those used in the base of the reference element (for further details, see for instance <30; 50>). The normal vector of the tangent plane is obtained by taking $\vec{g}_3 = \vec{g}_1 \wedge \vec{g}_2$. The norm of $\vec{g}_3$ is arbitrarily set at 1 (see fig. 1).

The contravariant components σ^{ij} of the Cauchy stress tensor $\boldsymbol{\sigma}$ are defined at each Gauss Point M in the current configuration using these covariant base vectors according to:

$$\boldsymbol{\sigma} = \sigma^{ij} \vec{g}_i \otimes \vec{g}_j \tag{2}$$

The Almansi strain tensor can also be defined in the contravariant current base vector taking:

$$\boldsymbol{\varepsilon} = \varepsilon_{ij} \vec{g}^i \otimes \vec{g}^j \tag{3}$$

2.1. Evaluation of the membrane states

In the literature, to denote the various states of the membrane (taut, slacked and wrinkled), three criteria based on the signs of the components σ_{I} and σ_{II} of the principal stresses and/or the principal strains ε_{I} and $\varepsilon_{\mathrm{II}}$ are now widely used (see table 1).

According to Liu et al. <21>, the stress criterion underestimates the state of "*slackness*" and the strain criterion underestimates the state of "*tautness*" of the membrane. Several authors <20; 51> have suggested that the mixed criterion seems to be the most useful means of differentiating between these

Membrane states	Stress criterion	Strain criterion	Mixed criterion
Taut	$\sigma_{II} > 0$	$\varepsilon_{II} > 0$	$\sigma_{II} > 0$
Wrinkled	$\sigma_{II} < 0$ & $\sigma_{I} > 0$	$\varepsilon_{II} < 0$ & $\varepsilon_{I} > 0$	$\sigma_{II} < 0$ & $\varepsilon_{I} > 0$
Slacked	$\sigma_{I} < 0$	$\varepsilon_{I} < 0$	$\varepsilon_{I} < 0$

Table 1: The three membrane states defined by the stress, strain and mixed criteria as a function of the principal stresses and strains.

states. Wang et al. <6> recently presented a new means of modelling these three states, taking the previous state obtained in the membrane and a combination between the stress criterion and the strain criterion. This new approach seems to be as effective as the mixed criterion but it requires the use of the Poisson's ratio, which restricts its use to material with linear elastic behaviour. In view of this constraint, the mixed criterion was adopted in the PS−DPS model. From a numerical point of view, a first computation without taking into account the wrinkles is carried out to determine these zones.

2.2. Principles underlying the PS−DPS model

As mentioned above in the Introduction, there are several ways of approaching wrinkles numerically. In the PS−DPS model, the aim is not to model the shape of the wrinkles, but to predict the consequences of the presence of wrinkles on the mechanical equilibrium of the membrane. From the practical point of view, the PS−DPS is intended to apply to a wrinkled structure, regarded as a unwrinkled planar membrane. The out-of-plane displacement caused by compressive stresses is simply approached like an in-plane contraction, as shown in fig. 1.

The PS−DPS model is based on two numerical assumptions. First, in

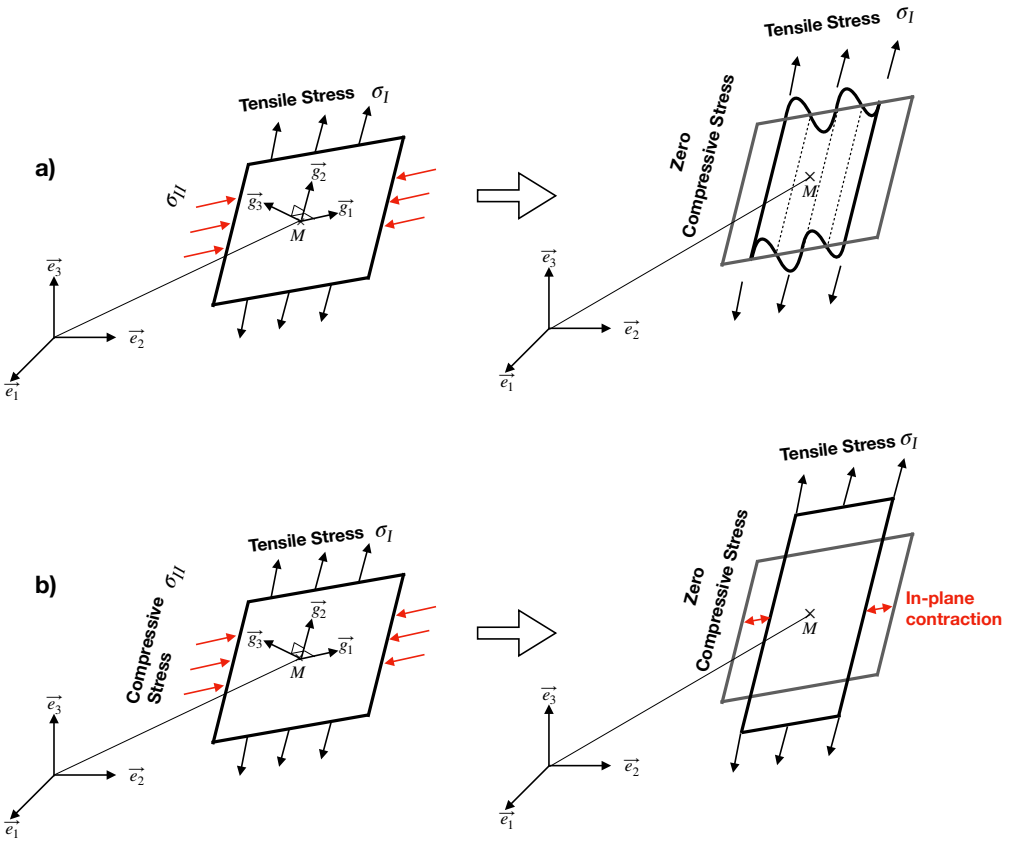

Figure 1: Diagram of the position and stress state of a Gauss point M in the membrane plane formed by $(\vec{g_1}, \vec{g_2})$ in the Cartesian coordinate system $\vec{e_i}$. a) Real membrane stress with wrinkles. b) Accounting for the behaviour of wrinkles with the PS−DPS model.

the case of any 3D behavioural law, a Newton-Raphson technique is used to impose a "Plane Stress" (PS) state on the membrane structures. In the second step, the assumptions of the TF theory, which we refer to here as the "Double Plane Stress" (DPS), are applied to the wrinkled part in a state of uniaxial tension on the plane of the membrane.

2.3. Membrane behaviour without any wrinkles: the PS state

During the equilibrium incremental, we assume that we have reached the end of an increment of time $t + \Delta t$, in which the kinematic displacements are

known, *i.e.* the 3D deformation state $\boldsymbol{\varepsilon}_{(t+\Delta t)}$, the increment of deformation $\Delta_t^{t+\Delta t}\boldsymbol{\varepsilon}$ between t and $t+\Delta t$, the strain rate tensor $\boldsymbol{D}_{(t+\Delta t)}$ and the 3D stress state $\boldsymbol{\sigma}_{(t+\Delta t)}$ are all known.

The first step in this approach consists in finding a PS state such that $\sigma^{3i} = 0$ as a function of the unknowns ε_{3i}, where $i = 1 \ldots 3$, at each Gauss point M. In this case, as $\vec{g}_3$ is assumed to be a principal direction (*i.e.* an eigenvector for stress and strain tensors) and $\varepsilon_{31} = \varepsilon_{32} = 0$, the sole condition which has to be found is:

$$\sigma^{33}(\varepsilon_{33}) = 0 \tag{4}$$

To obtain this no stress compression state $\sigma^{33}(\varepsilon_{33}) = 0$, which is denoted $\boldsymbol{\sigma}_{(int)}$, a scheme based on a three steps Newton-Raphson algorithm is used (see also the first algorithm scheme of the PS state in fig. 2):

1. The initial value of the strain tensor is such that $\varepsilon_{\gamma\eta_{(t+\Delta t)}}$ where $\gamma, \eta = 1, 2$ is due to the kinematic displacement of the membrane at the point M, taking: $\varepsilon_{31} = \varepsilon_{32} = 0$. These values will stay constant during the Newton loops during the n iterations. The unknown ε_{33} is initialized at the beginning of the initial step n=1, by: $\varepsilon^{(n=1)}_{33_{(t+\Delta t)}} = \varepsilon_{33_{(t)}}$

2. Do while $\| \sigma^{33}_{(int)} \| < e_1$ where e_1 is a given level of precision (in the loop on n):

   (a) evaluate $\sigma^{ij(n)}$ and $\dfrac{\partial \sigma^{ij(n)}}{\partial \varepsilon_{kl}}$ from the 3D behaviour

   (b) calculate $\delta\varepsilon_{33} = -\left[\dfrac{\partial \sigma^{33(n)}}{\partial \varepsilon_{33}}\right]^{-1} \sigma^{33(n)}$, resulting from the application of the condition eq. (4)

   (c) then $\varepsilon_{33(n+1)} = \delta\varepsilon_{33} + \varepsilon_{33(n)}$ and increment n as: $n = n + 1$

   (d) update the membrane thickness.

At the end of this first intermediate state "int", after convergence, the data obtained are:

- the 3D stress tensor $\boldsymbol{\sigma}_{(int)}$ that satisfies the first PS condition,
- the new thickness deformation $\varepsilon_{33_{(t+\Delta t)}}$ and the associated new thickness $h_{(t+\Delta t)}$ of the membrane.

3. In the case of an implicit scheme, the tangent matrix of the behavioural law is also calculated: $\left[\dfrac{\partial \sigma^{\alpha\beta}}{\partial \varepsilon_{\gamma\eta}}\right]$ where $\alpha, \beta, \gamma, \eta = 1, 2$ which includes the PS condition. Details of the calculation of the tangent matrix in the PS condition are given in appendix A.

Thanks to this process, the plane stress state can be applied to any type of mechanical behavior.

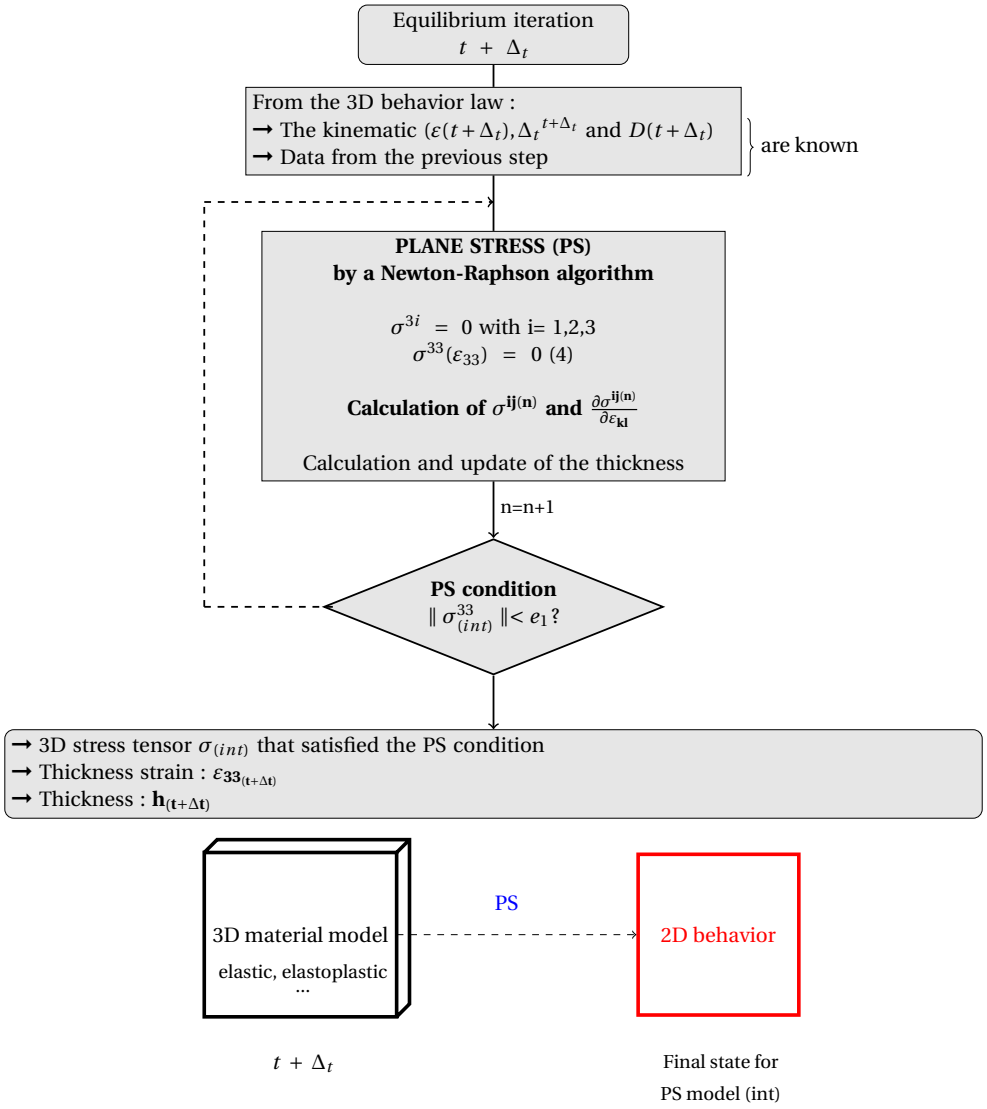

Figure 2: First algorithm used to define the PS state at a Gauss point on the membrane.

At the end of this state "*int*", the wrinkling areas are located in the membrane using the mixed criterion (see table 1). A new double plane stress (DPS) is then built into these wrinkles areas in order to release the compression by using a new Newton-Raphson algorithm (which will be discussed in the next section). The global equilibrium of the membrane is then updated with this new behaviour, which yields a new final stress $\boldsymbol{\sigma}_{(end)}$ and strain tensors $\boldsymbol{\varepsilon}_{(end)}$ that can be used in the next equilibrium iteration. In the tensile areas of the structure, the local state of the membrane satisfies the PS condition.

To define these wrinkled zones, eigenvalues of tensors $\boldsymbol{\sigma}_{(int)}$ and $\boldsymbol{\varepsilon}_{(int)}$ are calculated based on the notations $\sigma_{(int)_{\mathrm{I}}}$, $\sigma_{(int)_{\mathrm{II}}}$ which are the major and minor principal stresses, and $\varepsilon_{(int)_{\mathrm{I}}}$, $\varepsilon_{(int)_{\mathrm{II}}}$ which are the major and minor principal strains, respectively.

According to the mixed criterion (see section 2.1), the membrane could be in one of the following three states:

1. $\sigma_{(int)_{\mathrm{II}}} > 0$: the membrane is in a state of tension in all the directions on its median plane,

2. $\varepsilon_{(int)_{\mathrm{I}}} < 0$: the membrane lacks of tension in all the directions on its median plane,

3. $\sigma_{(int)_{\mathrm{II}}} < 0$: there are wrinkles in the direction of the eigenvector $\vec{V}_2$ associated with $\sigma_{(int)_{\mathrm{II}}}$.

2.4. Membrane with wrinkles: the PS−DPS Wrinkles Model

After determining the presence of wrinkles in the structure with the mixed criterion and the orientation of these wrinkles, the new stress and strain fields obtained with the DPS condition are determined using a new Newton-

Raphson algorithm. This DPS condition consists in imposing a new plane stress state in the direction of the wrinkles.

Take the eigenvector frame $\vec{V}_\alpha$ with $\alpha = 1, 2$, where $\vec{V}_1$ is the direction of the tension and $\vec{V}_2$ the transverse direction of the wrinkles. $\vec{V}_3$ is identical to $\vec{g}_3$ and gives a complete 3D eigenvector frame. In this frame, the presence of wrinkles must lead to $\sigma^{22} = 0$ and the PS model implies that: $\sigma^{33} = 0$. So the local behaviour is like a DPS constrain and the local stress state has to be studied again with the new conditions:

$$\sigma^{\alpha\alpha}\left(\varepsilon_{11}, \varepsilon_{22_{(mec)}}\right) = 0 \tag{5}$$

where $\alpha = 2, 3$ and a new unknown $\varepsilon_{22_{(mec)}}$ is introduced to denote the transverse mechanical strain, which differs from the kinematic deformation of the membrane $\varepsilon_{22_{(kin)}}$.

A Newton-Raphson scheme for the DPS state is therefore written in the frame $\vec{V}_i$ according to the following algorithm (see also this algorithm in fig. 3):

1. Initialization of the strain tensor component: $\varepsilon_{11_{(t+\Delta t)}}$ with the kinematic displacement of the membrane at the point M, taking $\varepsilon_{12} = \varepsilon_{31} = \varepsilon_{32} = 0$. These values will stay constant during the Newton loops on the n iterations. The unknowns are initialized by: $\left\langle \varepsilon_{22_{(t+\Delta t)}}, \varepsilon_{33_{(t+\Delta t)}} \right\rangle^{(n=1)} = \left\langle \varepsilon_{22_{(t)}}, \varepsilon_{33_{(t)}} \right\rangle$ for $n = 1$.

2. Do while $\| \left\langle \sigma^{22}_{(int)}, \sigma^{33}_{(int)} \right\rangle \| < e_2$ where e_2 is a given precision (loop on n):

   (a) evaluate $\sigma^{ij(n)}$ and $\dfrac{\partial \sigma^{ij(n)}}{\partial \varepsilon_{kl}}$ from the 3D behaviour

   (b) calculate $\langle \delta\varepsilon_{ff} \rangle = -\left[\dfrac{\partial \sigma^{ee(n)}}{\partial \varepsilon_{ff}}\right]^{-1} \sigma^{ee(n)}$ with e, f =2 and 3, because of the double conditions of eq. (5)

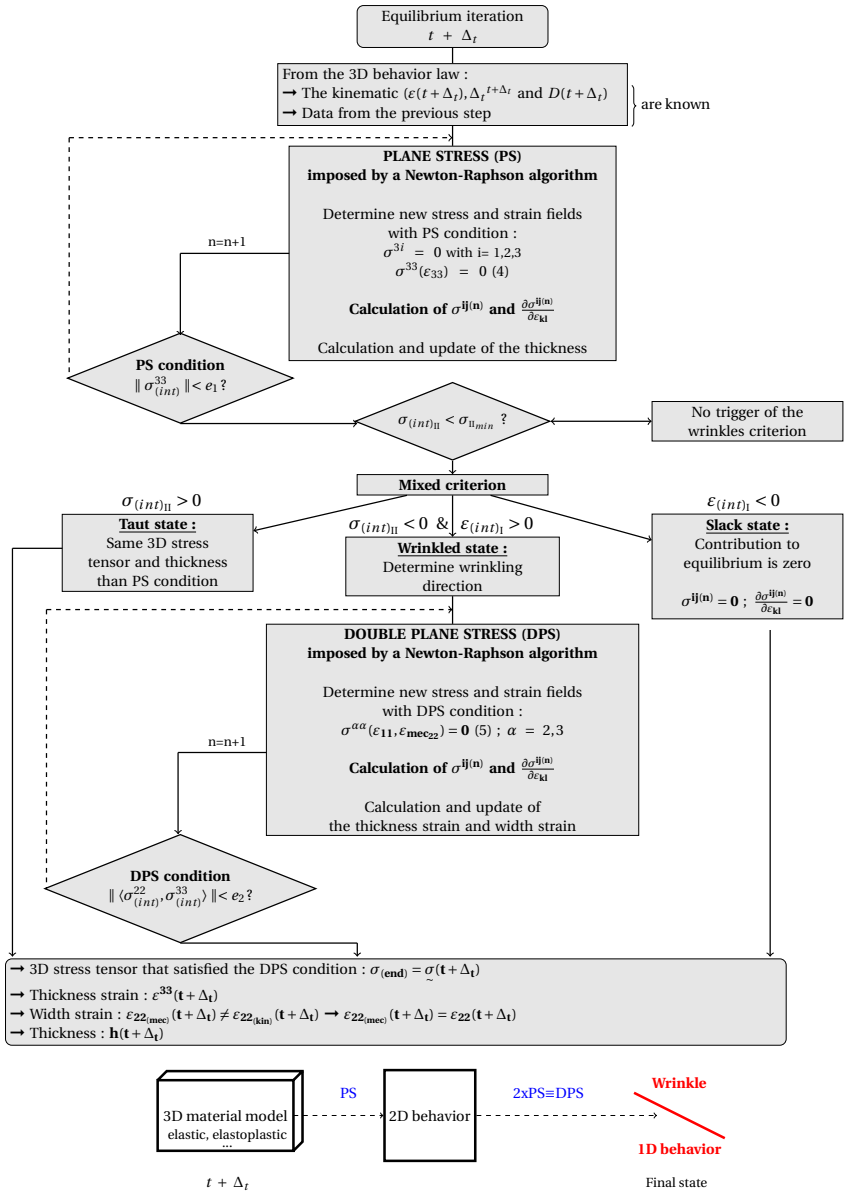

Figure 3: Total algorithm used to model the PS−DPS state with any type of 3D mechanical behaviour.

(c) then take $\varepsilon_{ff(n+1)} = \delta\varepsilon_{ff} + \varepsilon_{ff(n)}$ and increment n as: $n = n + 1$, with f =2 and 3

(d) update the membrane thickness.

At the end of the process, after convergence has been reached, which is denoted $\boldsymbol{\sigma}_{(end)}$, the following data are obtained:

- the 3D stress tensor $\boldsymbol{\sigma}_{(end)}$ that satisfies the DPS condition (*i.e.* only one value differs from zero: $\sigma^{11}_{(end)}$).
- the new thickness strain $\varepsilon_{33_{(t+\Delta t)}}$ and the new thickness $h_{(t+\Delta t)}$ of the membrane, the transverse mechanical strain $\varepsilon_{22_{(t+\Delta t)}}$ which is noted $\varepsilon_{22_{(mec)}}$. The difference between the strain $\varepsilon_{22_{(kin)}}$ due to the kinematic effects and the new $\varepsilon_{22_{(mec)}}$ is the presence of wrinkles.

3. as with the PS Newton scheme, in the case of an implicit scheme, the tangent behavioural matrix is also calculated based on: $\dfrac{\partial\sigma^{11}}{\partial\varepsilon_{11}}$ which includes the DPS condition. Details of the calculation of the tangent matrix of the DPS condition are given in appendix B.

The shape of the wrinkle is not simulated in the PS−DPS model, *i.e.* the membrane remains locally plane. The aim of this approach is simply to obtain the effects of the wrinkles. In this context, the kinematic deformation $\varepsilon_{22_{(kin)}}$ is the global deformation due to the undulation of the wrinkled membrane, and the mechanical deformation $\varepsilon_{22_{(mec)}}$ is the local behaviour of the material due to a single tension. $\varepsilon_{22_{(kin)}}$ could be much higher than $\varepsilon_{22_{(mec)}}$ and does not depend directly on the behaviour of the material, but mainly on the intensity of the undulation of the wrinkles, which is responsible of the global equilibrium.

Comment 1. Let us consider a length l of a membrane strip with a thickness h_0 and assume that a uniform simple tensile stress is applied along $\vec{g_2}$ as described in fig. 1. This stress makes it possible to obtain a unidirectional tensile state. In this case, wrinkles may appear in the direction $\vec{g_1}$ on the membrane. If no condition is imposed in the direction $\vec{g_1}$, the mechanical balance of the wrinkled membrane will be identical to that of the non-wrinkled structure, and it is possible to have the following cases:

- If the structure remains flat (no wrinkles), the new thickness and the width of the membrane will be those corresponding to the initial dimensions modified by the strains required to obtain zero transverse stresses.

- If the structure undulates, the width in the absence of any particular conditions along $\vec{g_1}$ can be arbitrary. In this case, the calculation of the tensile force required to achieve the balance of the structure creates an issue since the cross section (the thickness and width) can be arbitrary.

In this context, two types of thickness have to be considered:

1. The physical thickness $h_{(mec)}$ of the undulating membrane. This thickness will decrease with the tensile stress. In this paper, this thickness is also called the mechanical thickness.

2. The geometric thickness $h_{(kin)}$, which is associated with the geometric width of the corrugated strip $l_{(kin)}$ must yield a correct tensile force.

The length of the strip l is identical whether the membrane is wrinkled or not. On the other hand, the section of the non-wrinkled membrane given by the dimensions $h_{(mec)} \times l_{(mec)}$ must be identical to the section of the wrinkled

membrane $h_{(kin)} \times l_{(kin)}$. To obtain an identical volume, it is necessary to assume that:

$$h_{(kin)} = \frac{h_{(mec)} \times l_{(mec)}}{l_{(kin)}} \tag{6}$$

The geometric thickness will therefore tend to increase when wrinkles are present. This finding is described in the numerical shear test presented in section 4.1.

Comment 2. The given precisions e_1 and e_2 may be different. In sections 4 and 5, for example, the values of these parameters are $e_1 = e_2 = 1.10^{-3}$.

Comment 3. In principle, the PS−DPS model rules out the possibility of compressive stresses in the structure. In reality, infinitely small compression forces can accumulate in flexible structures, such as the plastic films used to make balloons. This admissible compression in the structure depends on many parameters such as the nature of the material used and its thickness. It can be observed with numerical simulations using shell elements as in the validation example tested in section 4.1. In the PS−DPS model, it is also possible to leave some compression in the structure by using a parameter named: $\sigma_{\text{II}_{min}}$ (see item item 3 of the algorithm in section 2.3). During a calculation, if the value of $\sigma_{(int)_{\text{II}}}$ is less than $\sigma_{\text{II}_{min}}$ then the mixed criterion is activated and all compressive stresses are eliminated. In the numerical examples presented in section 4.1, the value of the admissible compression is taken to be a very small value of $\sigma_{\text{II}_{min}} = -1.10^{-15}$.

Comment 4. In section 4, several numerical benchmarks will be simulated. The PS model presented in section 2.3 will also be compared with the PS−DPS model for analysing the effects of wrinkles on the local and global equilibrium.

3. The Dynamic Relaxation method

The complexity of the numerical modelling of stratospheric balloons is due in particular to the lack of flexural rigidity of the membranes and the occurrence of wrinkles on their surface. During an equilibrium search with a Newton-Raphson type algorithm, a singular stiffness matrix was obtained. Various methods such as the use of a numerical viscosity as in the Abaqus software <49>, for example, have been conventionally used to remove this singularity. With an implicit approach, it is difficult to accurately model the deployment phases which occur while the structures are being inflated; whereas explicit methods are more suitable for dealing with these phases involving large displacements. On the other hand, these explicit methods require a large number of computational steps and the final static balancing of the structure is often very time consuming. For this reason, the Dynamic Relaxation (DR) method has proven to be useful. This method has the advantages of the explicit approach while minimizing the computational times involved. This method, which has also been called pseudo-Dynamic method <44; 45; 52>, has been used by several authors for the simulations of pressurized balloons <40; 53–56> and wrinkling problems <11; 15>.

In line with our previous studies <52; 57; 58>, an original DR method was used here to deal with inflatable structure shape search problems. The main idea underlying the classical DR methods is that a static solution corresponds to the limit case of a damped dynamic system. Starting with the fundamental dynamic equation (eq. (7)), since the mass matrix intervenes only during the transient phase, the idea is to replace its real value by a fictitious value $[M']$, which is optimized with respect to the Courant-Friedrichs-Lewy (CFL) stability condition <59>.

$$[M']\{\ddot{X}'\} + [C']\{\dot{X}'\} + R\left(X, \dot{X}\right) = 0 \tag{7}$$

where $\{\ddot{X}'\}$, $\{\dot{X}'\}$ and $\{X\}$ are the acceleration vector, the velocity and the position of nodes, respectively. $[C']$ is the fictitious viscous damping matrix and $R\left(X, \dot{X}\right)$ stands for the residual internal and external forces. $\{\ddot{X}'\}$ and $\{\dot{X}'\}$ are regarded fictitious because these terms do not correspond to the real acceleration and the real velocity of the structure.

At convergence, the nodes tend to oscillate around the equilibrium position. The introduction of a damping term thus make it possible to approach the state of static equilibrium. The kinetic or viscous damping have been classically used for this purpose. These two types of damping stabilize the structure in very different ways <58>. In the present study, the kinetic damping method of stabilization, proposed by <44>, with which the overall balance of the structure can be obtained very quickly, was used.

In the case of the kinetic damping, an "undamped" movement is taken to occur with $[C'] = 0$ and the kinetic energy given in eq. (8) is used:

$$[M']\{\ddot{X}'\} + R(X, \dot{X}) = 0 \tag{8}$$

where the term $[M']\{\ddot{X}'\}$ is the generalized expression for the acceleration forces.

In the case of a conservative system, the kinetic energy reaches a maximum when the potential energy reaches a minimum. However, a minimum potential energy defines a state closely resembling the state of equilibrium. At each peak in the kinetic energy, the velocities are reset at zero and the computation is relaunched starting at the current position. This process, which consists in freezing the geometrical state of each peak in the kinetic energy, tends to dampen the oscillations. The addition of an artificial damping parameter leads the structure to gradually adopt a statically balanced form. The condition for stopping the calculation is defined by a fixed parameter, named ε_{DR}, which corresponds to the equilibrium state of the structure.

This parameter is calculated using the relation:

$$\max\left(\frac{\parallel \text{Residual static} \parallel_{\infty}}{\parallel \text{Reactions} \parallel_{\infty}}, \frac{\text{Kinetic energy}}{\text{Internal energy}}\right) \leqslant \varepsilon_{DR} \tag{9}$$

Comment. In section 4, the precision is set at $\varepsilon_{DR} = 1.10^{-4}$ which makes it possible to make novel comparisons with data in the literature. In section 5, a numerical test on the inflation of a stratospheric balloon is performed with the PS−DPS model and a non-linear behavioural law. In this case, the precision is set at $\varepsilon_{DR} = 5.10^{-3}$. This value is currently used by the CNES in all their balloon simulations because it gives precise local and global equilibria.

To solve the time problem, the method used here is based on the explicit Centered Finite Differences (CFD) method. The flow of the process is controlled by a fictitious time with an increment which is arbitrarily set at 1. The fictitious mass matrix is sized so as to satisfythe stability condition of eq. (10) more closely. For this purpose, a mass matrix calculated from the effective stiffness matrix is used, based on the Gershgorin theorem <45>. The mass matrix is updated only at specific times: at the start of the calculation and possibly after a damping step, which limits the time required to perform the computation. The mass matrix is calculated here only at the beginning of the simulation, taking:

$$m_i = \frac{\lambda \Delta t'^2}{2} S_i \rightarrow S_i = \sum_j \mid K_{ij} \mid \tag{10}$$

where m_i is the mass at node i, $\Delta t'$ is the fictitious time, S_i is calculated from the matrix K_{ij} which is the local stiffness matrix of each elements. S_i is calculated by taking the maximum value of the sum of the absolute values of the stiffness along the three axes of the Cartesian coordinate system. This maximum is applied in all the three directions. An increase occurs in the three eigenvalues obtained via the Gershgorin theorem applied locally to

each matrix <45>. λ is an adjustable parameter used to compensate for the instability of the schema resulting, for example, to the approximation of Gershgorin's theorem.

4. Numerical experiments

To investigate the performances of the present wrinkling model, several numerical benchmarks are modelled here and compared with data presented in literature.

First, by reproducing shear and torsion tests, structures subjected to in-plane loading are studied. The deployment of a square cushion is then carried out in order to test the validity of the model on a structure resembling that of stratospheric balloons. These complementary tests have been frequently used in previous studies on wrinkling models. In some cases, the membrane shifts locally from a wrinkled to a taut state (in torsion and cushion tests). In other cases, the membrane is completely wrinkled (either in one direction or in all directions), as in shear tests. In shear and torsion tests, an isotropic elastic law is used, and these tests are carried out under small strains, as performed in literature. In the case of the inflation of a square cushion, finite strains and elastic behaviour are first tested, but a hyperelastic model is then used to analyse the responses of the PS−DPS model with this non-linear behaviour.

4.1. Rectangular membrane under shear loading

A two-dimensional rectangular membrane under shear loading was first tested. This test has been widely used in the literature <3; 4; 6; 17; 60–62>. The solutions obtained with the PS and PS−DPS models were compared with numerical and experimental results previously obtained with an elastic law.

The geometry, loading conditions and material parameters used in this shear test are presented in fig. 4. A 0.025 mm thick 2D rectangular membrane (the plane of the membrane) measuring 380 mm x 128 mm in the XY plane was fixed at the lower edge, while the upper edge could move only in the horizontal direction. The geometry was meshed with 300 linear triangular membrane elements. These elements include one Gauss point and finite transformations (*i.e.* large displacements and deformations) were taken into account. The parameters λ used in the DR method were set at 2.

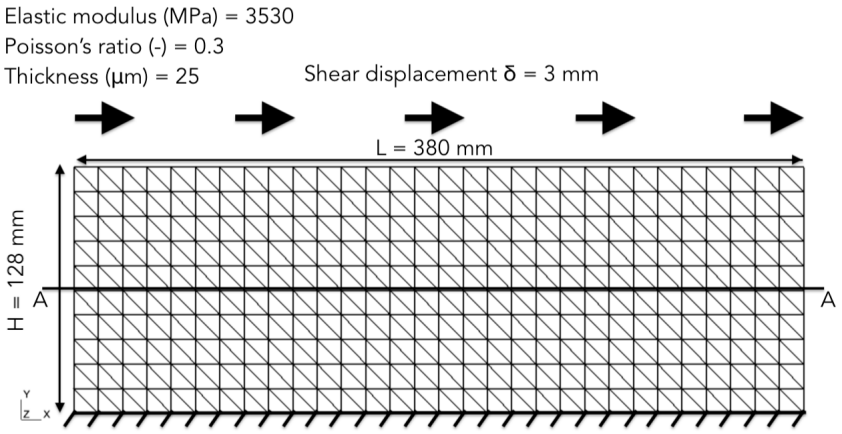

Figure 4: Membrane properties and kinematic boundary conditions in shear test with 300 linear triangular membrane elements performed with the PS and the PS−DPS models.

The flat membrane was loaded with a prestress with a magnitude of 1.5 N/mm^2 in the $Y-$direction to introduce an initial stiffness. The prestress was then held constant while the upper edge was gradually moved in the horizontal direction until this movement had covered a distance of +3 mm (see fig. 4).

In order to compare our results with data in the literature, this test was also simulated with shell elements in Abaqus <49> using the same method presented by Wong and Pellegrino in <3>. In this case, this simulation was

performed by taking 3960 S4R5 shell elements. As with membrane elements in Herezh++, a 1.5 N/mm^2 prestress was prescribed on the upper side of the rectangular membrane in order to induce an initial stiffness. After calculating the first buckling modes, the out-of-plane displacements caused by these modes were imposed like imperfections in addition to the boundary conditions of displacement of 3 mm in the $X-$direction. If the shell mesh is sufficiently fine, this method gives the shape of the wrinkles and eliminates the compression stresses due to the wrinkles.

The shear forces applied to the membrane using the PS, PS−DPS and shell models are presented and compared in fig. 5a as a function of the shear displacement.

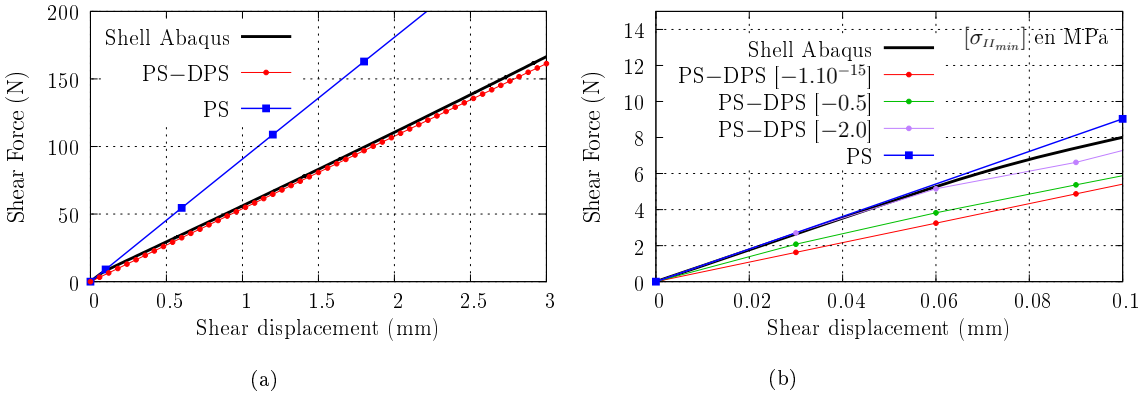

Figure 5: (a) Comparison of shear force/displacement relationships obtained using the shell model, the classical PS membrane model and the PS−DPS wrinkle model. (b) Zoom of the beginning of the shear force/displacement relationship showing the influence of the compressive stress $\sigma_{\mathrm{II}_{min}}$ (indicated in brackets) used in the PS−DPS model.

The initial in-plane shear stiffness of the shell model is approximately equal to 101 N/mm, which corresponds to the value given by Wong and Pellegrino. This stiffness obtained with the shell model decreases quickly at a value of 55 N/mm, showing a similar trend to that observed with the

PS−DPS model. This loss of stiffness is due to the development of wrinkles on the structure <3>. The PS membrane model does not account for the softening associated with the formation of wrinkles. Contrary to what occurs with the shell model, the relationship between force and displacement remains linear with the PS−DPS model, with which no compression by default can be included in its formulation. However, as explained in the Comment 3 in section 2.4, it is possible in the PS−DPS model to control the compressive stress state with the parameter $\sigma_{\mathrm{II}_{min}}$. Figure 5b shows the influence of the compressive stress parameter $\sigma_{\mathrm{II}_{min}}$ on the initial stiffness at the beginning of the shear-displacement curve. By default, this value was set at -1.10^{-15} MPa and in this case, during the initiation of buckling, the stiffness remains linear, contrary to what is predicted by the shell model. When this compression stress value is increased to almost 2 MPa, the PS−DPS model is then reflect the initial decrease in the stiffness, as observed with the shell model used by Wong and Pellegrino.

The principal stresses σ_{I} and σ_{II} across the middle of the membrane (see cross section A-A in fig. 4) are plotted in fig. 6a. This distribution of the principal stresses is compared with that obtained with the Abaqus shell model using 3960 S4R5 elements, the membrane model proposed by Deng and Pelegrino <38> and the PS−DPS model. The PS−DPS model gives results which are consistent with the Abaqus shell solution and the membrane wrinkling model previously studied in the literature. The minor principal stress σ_{II} is null in all these cases.

According to Deng and Pellegrino <38>, the orientation of wrinkles is equal to 45° at the centre of the membrane. The major principal strain ε_{I} and the major principal stress σ_{I} are exerted in the same direction as the

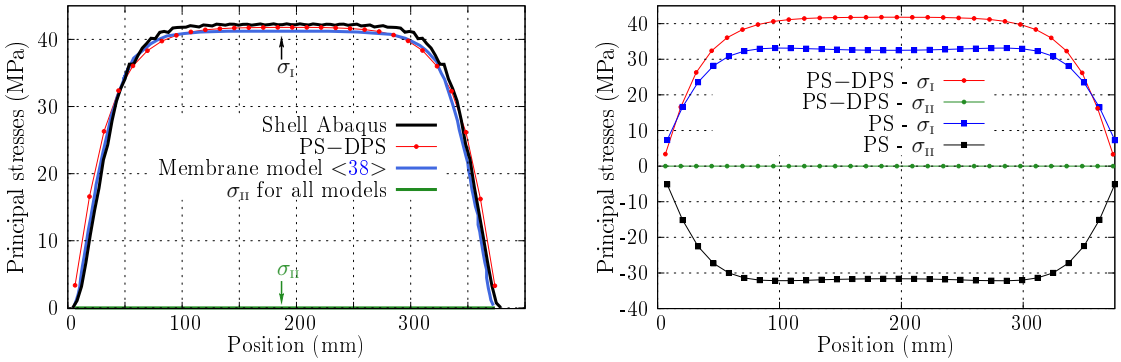

(a) (b)

Figure 6: (a) Distribution of the principal stresses σ_I and σ_{II} along the middle of the membrane for the Abaqus shell model, the membrane model presented in <38> and the PS−DPS model. (b) Comparison of these stresses between our PS membrane model and the PS−DPS model.

wrinkles. The following equations can be used to determine σ_I in this region:

$$\varepsilon_I = \frac{\lambda}{2} \text{ and } \sigma_I = E \times \varepsilon_I \tag{11}$$

where $\lambda = \frac{\delta}{H}$ is the elongation along X, δ is the horizontal displacement imposed, H is the height of the membrane (see fig. 4) and E is the Young's modulus.

Based on these equations, Wong and Pellegrino <63> have established that this major principal stress, is equal to 41.37 MPa. With the PS−DPS model, a value of 41.79 MPa is obtained, amounting to a difference of 1%. Figure 6b gives the major and minor principal stresses obtained with the PS and PS−DPS models in order to show the impact of the wrinkles on the local equilibrium of the structure. With the PS model, the major principal stress σ_I is lower than in the PS−DPS model, giving a difference of 20.7% and a minor principal stress of $\sigma_{II} \approx -30$ MPa is obtained. This value of σ_{II} was also obtained by Jarasjarungkiat et al. <19> with a classical PS membrane model.

As described in section 2.4, the PS−DPS model makes it possible to account for the wrinkles in a membrane structure without modelling the out-of-plane displacement. The mechanical strain that the structure actually undergoes is different from the geometric strain caused by the wrinkles. As mentioned above, the geometrical thickness $h_{(kin)}$ is due to the presence of wrinkles and the mechanical thickness $h_{(mec)}$ is equivalent to the physical thickness. The mechanical and the geometrical thicknesses obtained along the section of the membrane at the end of the shear test are compared in fig. 7.

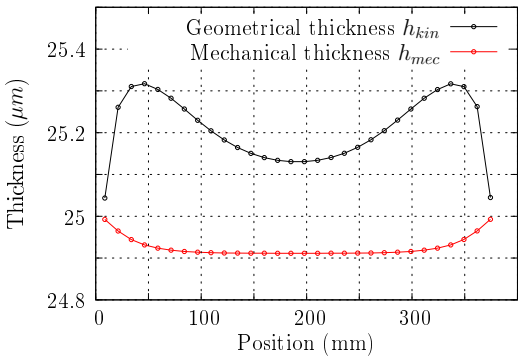

Figure 7: Distribution of the geometrical thickness $h_{(kin)}$ and the mechanical thickness $h_{(mec)}$ along the middle of the membrane in the case of the PS−DPS model.

The geometrical thickness $h_{(kin)}$ increases in the wrinkled area due to the out-of-plane movement caused by the formation of the wrinkles, whereas the mechanical thickness is negative because the membrane is in a uniaxial tensile state. The distribution of geometric thickness consists of two high peaks ($h_{(kin)} \approx 25.3\ \mu m$) located near the free edges on both sides of the membrane. The geometrical thickness decreases in the middle of the membrane, but it is still greater than the initial thickness ($h_{(kin)} \approx 25.1\ \mu m$). Similar results were obtained experimentally by Wong et al. <62> in a study in which they subjected a rectangular membrane to a state of simple shear. These authors

reported that the out-of-plane deflection was greater near to the free edges on both sides of the membrane. In the middle, the out-of-plane displacement decreased and the region was characterised by fairly uniform wrinkles.

To conclude this part, although the PS−DPS model is not suitable for modelling the shape of wrinkles, the geometrical thickness is a good indication to the wrinkling pattern in the membrane. This shear test was the first step in the validation of the PS−DPS wrinkle model. The torsion test which will now be described was performed in order to analyse the response of the PS−DPS model under these new loading conditions with an elastic law.

4.2. Torsion test on an annular membrane

In this numerical test, an annular membrane is attached to a rigid hub along the inner edge and to a guard ring along the outer edge as shown in fig. 8. The rotation of the rigid disc causes wrinkling of the membrane <12>. Two tests, classically used in the literature, are simulated: the first is a torsion test without any initial prestress <4; 19> and an initial prestress is added in the second test <7; 27>. In both cases, an analytical solution is presented in <64> and theses solutions are also obtained with a Python script. In the case of the prestress torsion test, the membrane shifts locally from a one-directional wrinkled state to a stretched state (devoid of wrinkles). The aim of this prestress torsion test is to determine the robustness of the PS−DPS model when moving from one state to another. The value of parameter λ adopted in the DR method was set at 4 in all these torsion tests.

4.2.1. Torsion without any prestress

In this test, all translations of the outer nodes are fully constrained and the inner rigid disk is rotated clockwise by the angle θ (see fig. 8). The mesh is composed of 180 quadrangular membrane elements with linear interpolation.

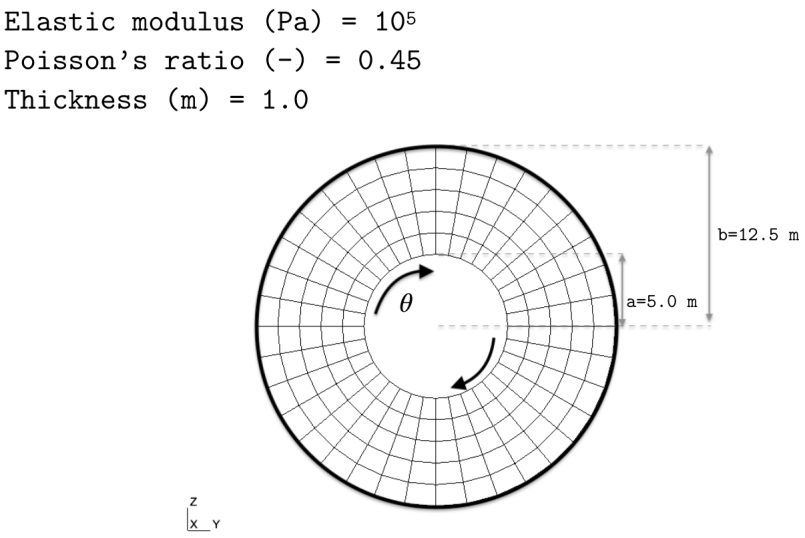

Figure 8: Geometry, physical properties and load at the inner edge of the annular membrane.

These elements include four Gauss points and involve finite transformations (*i.e.* large displacements and deformations). The dimensions and loading conditions of the membrane studied here are given in fig. 8 as well as the properties of the linear elastic law used.

In the studies by Jarasjarungkiat et al. <4; 19>, the angle θ imposed on the inner rigid disk is 10°. However, with this angle, the strain values obtained are significantly greater than 10% which results relatively large strains. As explained above in the Introduction, the PS−DPS model involves the Almansi strain measure whereas in literature, the Green strain measure has been generally used so far with wrinkle models. As shown in fig. 9, the directions of the major principal stresses are nevertheless compatible with those reported in <12; 65> with an angle of 10°. In order to compare the numerical results obtained with the PS−DPS model and data presented in previous numerical studies, an analytical solution given by Mikulas <64>

in the case of small deformations was used with an angle of 0.728°, which corresponds to a moment equal to 10^5N.m. This small angle makes it possible to compare data obtained in the case of small rotations with strain fields of less than 10%.

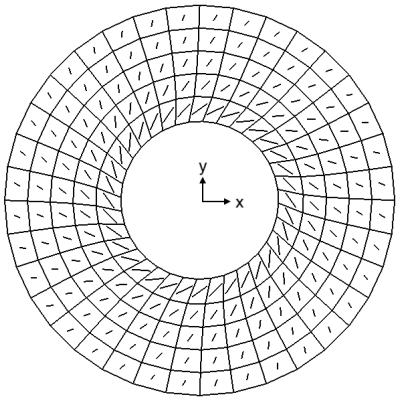

Figure 9: Deformed mesh with representation of the principal stress vectors involving an angle $\theta = 10°$ in the case of a linear elastic material.

In this case, wrinkling occurs over the entire membrane as soon as an angle is applied to the hub. Based on equations given in <64>, it is possible to compute the stress state in the membrane in two steps.

The first step consists in determining the value of the constant C_2 which satisfies the boundary conditions on the edges of the membrane, according to the following equation:

$$\frac{1}{\frac{4\pi^2 t^2 {C_2}^2 a^2}{M^2} - 1} + \log\left(\frac{4\pi^2 t^2 {C_2}^2 a^2}{M^2} - 1\right) - \frac{1}{\frac{4\pi^2 t^2 {C_2}^2 b^2}{M^2} - 1} - \log\left(\frac{4\pi^2 t^2 {C_2}^2 b^2}{M^2} - 1\right) = 0 \tag{12}$$

where a is the inner radius, b is the outer radius, t is the membrane thickness and M is the torque applied.

When the constant C_2 is known, the second step consists in calculating

the radial σ_r and tangential stresses σ_θ based on the following equations:

$$\begin{cases} \sigma_r &= \dfrac{1}{r}\sqrt{C_2 - \dfrac{M^2}{4\pi^2 t^2 r^2}} \\ \sigma_\theta &= \dfrac{M^2}{4\pi^2 t^2 r^4}\dfrac{1}{\sigma_r} \end{cases} \tag{13}$$

where r is the radial position in the membrane.

To determine the angle of the wrinkles α, as shown in fig. 10, the stress field can be written as follows:

$$\begin{cases} \alpha &= \arcsin\left(\dfrac{M}{2\pi t\sqrt{C_2}r}\right) \\ \sigma_{\text{I}} &= \dfrac{\sigma_r}{\cos^2\alpha} = \dfrac{\sigma_\theta}{\sin^2\alpha} \end{cases} \tag{14}$$

This same problem has been solved using TF theory by Reissner <66>, who established that the tension lines start from the inner edge, and because of the symmetry, each of these lines forms along the inner edge the same angle with the radius from the origin (fig. 10).

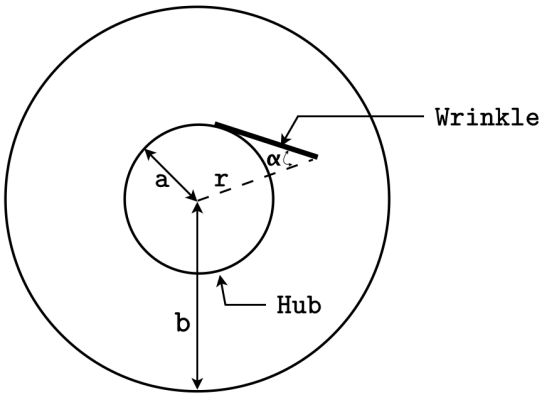

Figure 10: Angles of wrinkles α as described in <64>.

One simulation was performed with the PS−DPS model with an angle θ equal to 0.728° and compared with this analytical solution, as shown in fig. 11. The results show the evolution of the major principal stress σ_{I} along

the radius of the structure. The PS−DPS model predicts the same evolution of the decrease of the principal stress along the radius as the analytical solution. The PS−DPS model can be used to simulate a completely wrinkled membrane state. The next test consists in adding an initial prestress to the torsion test.

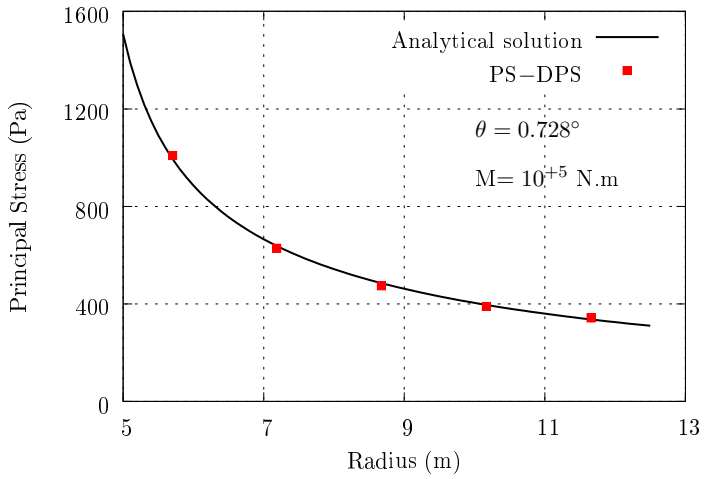

Figure 11: Comparison between the results obtained with the analytical model <64> and the PS−DPS model on the evolution of the major principal stress σ_1 with $\theta = 0.728°$ and 180 quadrangular membrane elements.

4.2.2. Torsion with prestress

The rigid hub was then subjected to a torque loading M and rotated through an angle ϕ, and this membrane was subjected to a uniform prestress σ_0. The geometric and elastic material parameters used in this test are presented in fig. 12a.

When the torsion loading was applied by increasing the moment M, wrinkles began to form around the hub up to some radius R, as explained for example by Akita et al. <27>. The two meshes, described in fig. 12b, with quadrangular membrane elements, with linear interpolation and four Gauss

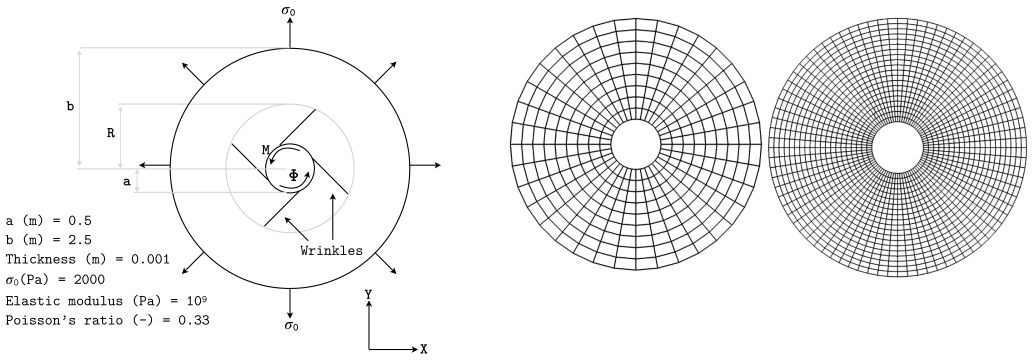

(a) (b)

Figure 12: a) Dimensions and material properties in the annular membrane test under torque applied to the inner edge with prestress σ_0. b) Coarse (324 elements) and fine (1600 elements) meshes used to simulate this test.

points, are tested in order to determine the influence of the finite element size. The coarse mesh was composed here of 324 elements and the fine mesh, of 1600 elements.

The analytical solution of this problem presented in <64; 67> has been used by several authors <27; 68>. In this analytical solution, the relation between the wrinkle radius R and the moment M is given by the following equations. The quadratic eq. (15) has to be solved to determine the constant C_1. This constant C_1 can be used to calculate C_2 with eq. (16). Lastly, we checked the values of this constant with eq. (17).

$$C_1{}^2 - \left[1 + 2C_1\left(\frac{a^2}{b}\right)\right]^2 \overline{R}^4 + \overline{M}^2 = 0 \tag{15}$$

$$C_2 = (\overline{R} + [\frac{1}{\overline{R}} + 2\overline{R}\frac{a^2}{b})]C_1)^2 + (\frac{\overline{M}}{\overline{R}})^2 \tag{16}$$

$$\frac{1}{A} + \frac{1}{B} - ln(\frac{B}{A}) - \frac{2}{3} = 0 \tag{17}$$

where $\overline{M} = \dfrac{M}{2\Pi\,\sigma_0\,t\,a^2}$; $A = \dfrac{C_2}{\overline{M}^2} - 1$; $B = \overline{R}^2\dfrac{C_2}{\overline{M}^2} - 1$ in which $\overline{R} = \dfrac{R}{a}$, R being the radial extent of the wrinkled region, C_1 and C_2 are constants which can be used to calculate the stress field, t is the thickness of the film and a and b are the inner and outer radii, respectively.

The relation between the moment M and the twist angle ϕ is given by:

$$\overline{\phi} = \frac{3\overline{M}}{8(1-\frac{a^2}{b^2})}\left[\frac{\frac{1}{\overline{R}^2}-1}{B} + ln\left(\frac{B}{A}\right) + \frac{1}{\overline{R}^2} - \frac{8}{3}\left(\frac{a^2}{b^2}\right) + \frac{5}{3}\right] \tag{18}$$

where:

$$\phi = \frac{4\overline{\phi}\sigma_0\left(1-\frac{a^2}{b^2}\right)}{3E} \tag{19}$$

In the simulation, the angle ϕ determined by eq. (19) is imposed on the inner radius a.

The moment applied causes the occurence of wrinkles on a certain radius denoted $\overline{R}$. Contrary to the torsion test without any prestress presented in section 4.2.1, the structure falls into two areas. With values of $\overline{R}$ =1.2, 1.4 and 1.6, the membrane is in a wrinkled state in one direction and beyond these values, the membrane is stretched. Comparisons are made here only with these values of $\overline{R}$.

After solving the previous equations, the ratios $\frac{\sigma_{\mathrm{I}}}{\sigma_0}$ and $\frac{\sigma_{\mathrm{II}}}{\sigma_0}$ between the principal stresses and the prestress (with $\sigma_{\mathrm{I}} > \sigma_{\mathrm{II}}$) are given in the wrinkled zone $\overline{r} < \overline{R}$ according to the following relations:

$$\begin{cases} \dfrac{\sigma_{\mathrm{I}}}{\sigma_0} & = \dfrac{\frac{C_2}{\overline{r}}}{\sqrt{C_2 - \frac{\overline{M}^2}{\overline{r}^2}}} \\ \dfrac{\sigma_{\mathrm{II}}}{\sigma_0} & = 0 \end{cases} \tag{20}$$

where $\overline{r} = \frac{r}{a}$.

These ratios are obtained in the wrinkle-free zone ($\overline{r} \geq \overline{R}$), where:

$$\begin{cases} \dfrac{\sigma_{\mathrm{I}}}{\sigma_0} &= 2C_1 \dfrac{a^2}{b^2} + 1 + \sqrt{\dfrac{C_1^2 + \overline{M}^2}{\overline{r}^2}} \\ \dfrac{\sigma_{\mathrm{II}}}{\sigma_0} &= 2C_1 \dfrac{a^2}{b^2} + 1 - \sqrt{\dfrac{C_1^2 + \overline{M}^2}{\overline{r}^2}} \end{cases} \tag{21}$$

Figs. 13a to 14b give the ratios $\frac{\sigma_{\mathrm{I}}}{\sigma_0}$ and $\frac{\sigma_{\mathrm{II}}}{\sigma_0}$ as a function of $\overline{r} = \frac{r}{a}$, respectively, with various torques values in the case of coarse and fine meshes.

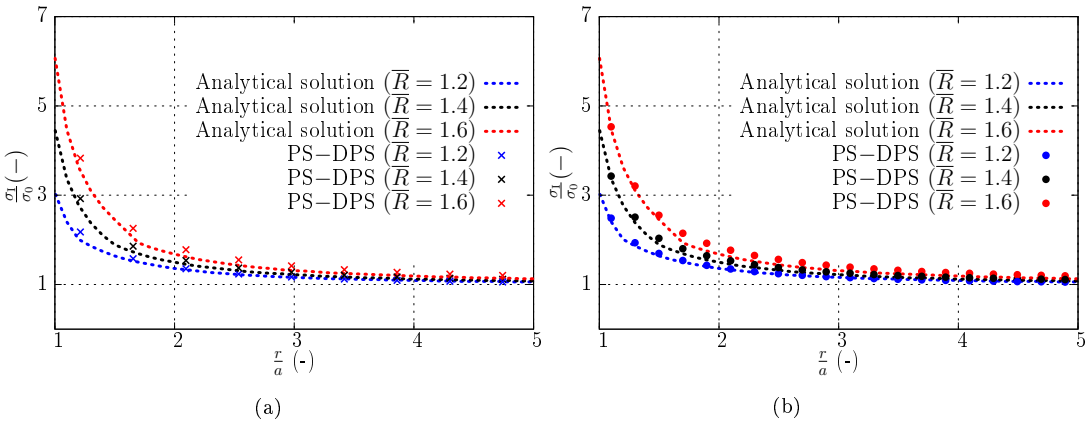

Figure 13: Comparison between the analytical solution and the results obtained with the PS−DPS model for $\frac{\sigma_{\mathrm{I}}}{\sigma_0}$, depending of the radial position $\frac{r}{a}$. (a) Coarse mesh (324 elements). (b) Fine mesh (1600 elements).

The switch between the wrinkled area and the stretched area is shown in fig. 14. The ratio $\frac{\sigma_{\mathrm{II}}}{\sigma_0}$ is equal to zero when the structure is wrinkled, but increases along the radius in the stretched area. Figure 13 shows that the evolution of $\frac{\sigma_{\mathrm{I}}}{\sigma_0}$ is accurately predicted by the PS−DPS model with both coarse and fine meshes. However, in the case of the evolution of $\frac{\sigma_{\mathrm{II}}}{\sigma_0}$, the solution obtained with the fine mesh resembles the analytical solution slighlty more closely than that obtained with the coarse mesh. In fact, the influence of the mesh is quite weak on the results of this test with the PS-DPS model. The

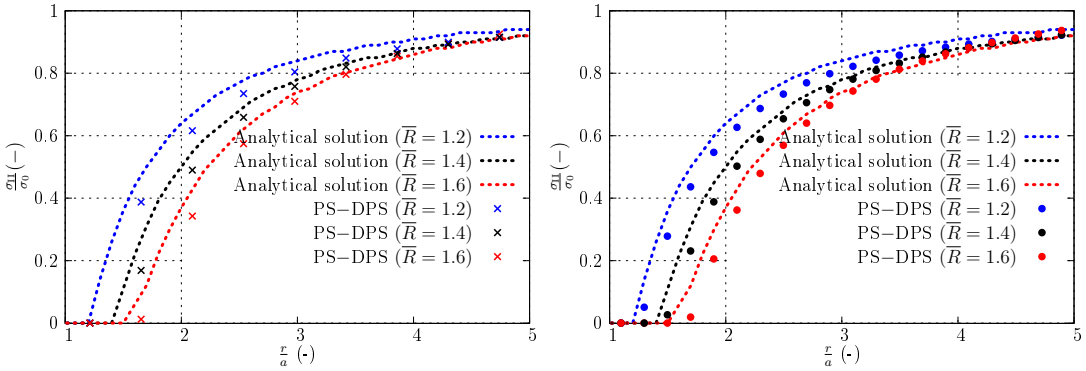

Figure 14: Comparison between the analytical solution and the results obtained with the PS−DPS model for $\frac{\sigma_{II}}{\sigma_0}$, depending of the radial position $\frac{r}{a}$. (a) Coarse mesh (324 elements).(b) Fine mesh (1600 elements).

results here resemble the analytical solutions, even with a mesh composed of only a few elements, which is not the case with a shell mesh, as observed in the shear test presented in section 4.1.

4.3. Inflation of a square cushion with an elastic law

In this example, the efficiency of the PS−DPS model is tested in the case of an inflatable structure. This test has been extensively studied with an elastic law in the literature <4; 19; 20; 35; 43>. It consists in gradually inflating a flat square elastic isotropic membrane, increasing the constant pressure up to 5 kPa. The material properties and dimensions of the undeformed cushion are given in fig. 15.

By applying appropriate boundary conditions in the horizontal mid-plane, it is only necessary to model one upper quarter of the cushion. This eighth of the square cushion was simulated with various mesh sizes. The initial discretization was 4×4 and refined as 5×5, 8×8 and 10×10 quadrangular elements with linear interpolation and 4 Gauss points, consecutively. Figs

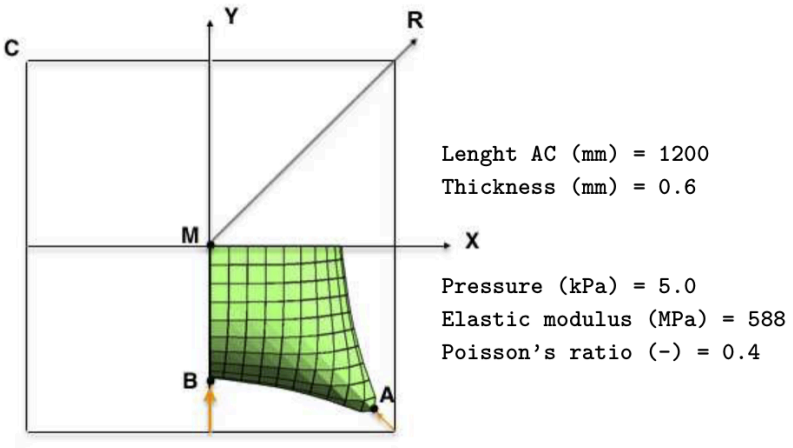

Figure 15: Membrane geometry and material properties of the inflated square cushion test.

16a and 16b show the deformed mesh given by the PS−DPS and PS models, respectively (showing the symmetrical parts of the meshes). The parameter λ used in the DR method was set in this case at 1.5.

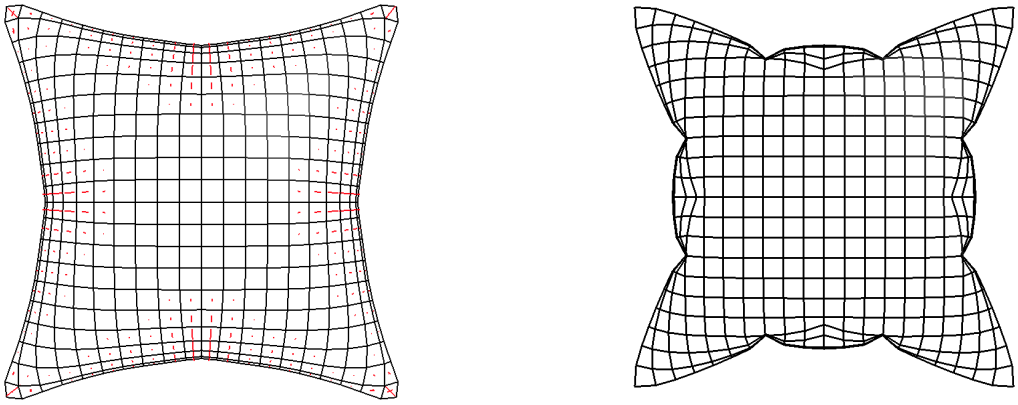

(a) (b)

Figure 16: Deformed shape of the inflated square cushion testes at a pressure of 5 kPa with a mesh consisting of 5×5 elements. (a) With the PS−DPS model showing the wrinkled zones (in red). (b) With the PS model without taking the wrinkles into account.

Previous authors have compared four quantities: the distribution of the stresses along in the direction X, the major principal stress and the vertical displacement occurring in the centre M and the displacement in the direction Y at point B (see fig. 15). The results obtained with PS−DPS model were

compared with data previously published in the literature <4; 19; 20; 35; 43> and simulations performed using the "No compression" model implemented in Abaqus. This model approaches the elastic behaviour by first solving for the principal stresses assuming linear elasticity and then setting the appropriate principal stress values to zero. The associated stiffness matrix components were also set at zero. "No compression" model can be rather unstable, which explains why convergence problems are liable to occur.

In figs 17a and 17b, data obtained in previous studies and those obtained with the PS−DPS model are compared in terms of the displacement of points M and B. The results obtained with the PS−DPS model are almost identical to those obtained with the models presented in <4; 19; 20; 35; 43>. These figures show that the shape of the cushion is accurately predicted at points M (in the stretched area) and B (in the wrinkled area) by the PS−DPS model. Note that the "No compression" Abaqus model gives strange displacements at point B in the wrinkled area, as previously reported by Contri and Schrefler <35>. These models involve the used of a static implicit scheme to solve the wrinkling problem. An equilibrium position of the membrane is first determined with active compressive stresses and tensile stresses. If at least one such principal stress is found to be compressive in an element, a new stress state with only the tensile stresses active is obtained. These models do not seem to be as effective as the PS−DPS model.

In fig. 18a, the major principal stress σ_{I} occuring at point M, depending of the mesh size used, is compared with results obtained in <19; 43>. The stress states predicted with the PS−DPS model show good agreement with these previous data. Figure 18b shows the evolution of the stresses σ_{11} and σ_{22} in the direction X in the cushion predicted by the PS−DPS model and the membrane model presented by Lee et al. <11>, in the only study in

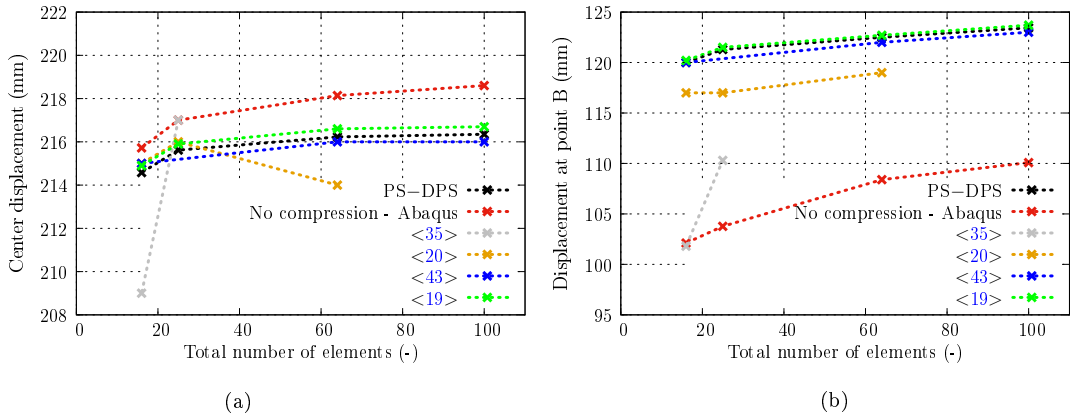

Figure 17: Displacement at the centre (point M) (a) and point B (b) predicted with various mesh sizes (4×4, 5×5, 8×8 and 10×10 elements) in comparison with data obtained in <4; 19; 35; 43>, the "No compression" model and the PS−DPS model.

the literature to deal with this evolution. The results give a picture of the wrinkling behaviour and the tensile area in the cushion. σ_{22} is equal to zero and σ_{11} is almost equal to 1.5 MPa in the wrinkled area. In the taut area, the values of σ_{22} and σ_{11} both increase. The values of σ_{22} and σ_{11} are equal in the centre of the cushion (position $\approx$ 25 mm). The stress field predicted with the PS−DPS model is similar to that obtained in previous studies.

This test finishes the validation section of the PS−DPS model with a linear elastic law in comparison with literature cases. These previous tests showed the ability of the PS−DPS model to account for the formation of wrinkles in flexible structures. The tests described in the next section were performed on the PS−DPS model with a non linear law in order to determine the effects of the mechanical behaviour on the shape of the cushion and the local equilibrium.

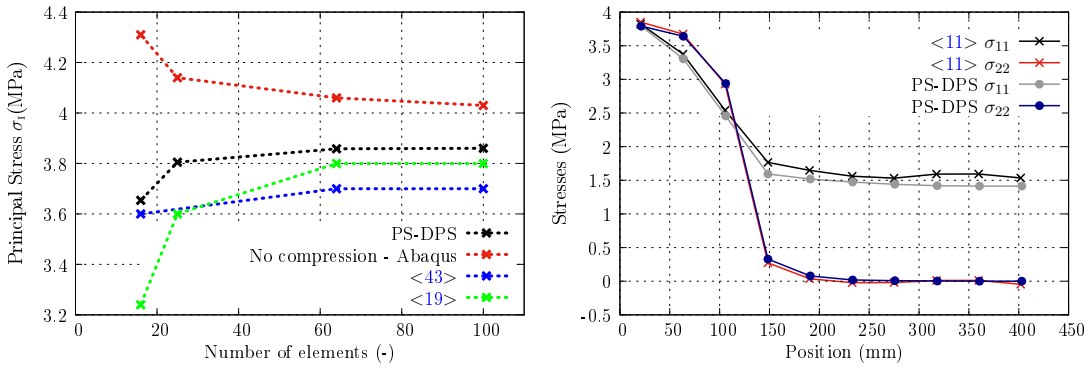

(a) (b)

Figure 18: (a) Major principal stress σ_I at point M with meshes consisting of 4×4, 5×5, 8×8 and 10×10 elements in comparison with data presented in previous studies <19; 43>, the "No compression" model and the PS−DPS model. (b) Comparison between the stresses σ_{11} and σ_{22} occuring in the Xdirection of the cushion obtained in <11> and with the PS−DPS model.

4.4. Inflation of a square cushion with a non-linear law

Stratospheric balloons are made of very fine plastic films showing complex mechanical behaviour. In order to approach this non linear behaviour, a simulation was performed on the inflation of a square cushion using the PS−DPS model and the original hyperelastic law initially defined by Favier et al. <69>. This hyperelastic part was previously used in a study of Zrida et al. <70> to simulate the behaviour of polymers.

The hyperelastic potential W involved in this law was defined on the basis of four material parameters, using the invariants of the Almansi measure $\boldsymbol{\varepsilon}$ according to the relation:

$$W = \frac{K}{6}\ln^2(V) + \frac{Q_{0r}^2}{2\mu_0}\ln\left(\cosh\left(\frac{2\mu_0 Q_\varepsilon}{Q_{0r}^2}\right)\right) + \mu_\infty Q_\varepsilon^2 \qquad (22)$$

where in the case of a shear test, μ_∞ denotes the final slope of the stress τ-strain γ curve, $\mu_0 + \mu_\infty$ denotes the initial slope τ versus γ and Q_{0r} stands

for the level of the final tangent to the curve (*i.e.* the intersection between the final tangent and the vertical stress axis) (for details of these material parameters, see fig. 19). K is the bulk modulus, on which the changes in volume mainly depend. V stands here for the relative changes in volume and $Q_{\bar{\varepsilon}}$ denotes the intensity of the deviatoric part of $\boldsymbol{\varepsilon}$:

$$Q_{\bar{\varepsilon}} = (2\bar{\Pi}_{\bar{\varepsilon}})^{1/2} \text{ with } \bar{\Pi}_{\bar{\varepsilon}} = \frac{1}{2} trace\,(\boldsymbol{\varepsilon}.\boldsymbol{\varepsilon}) - \frac{(trace(\boldsymbol{\varepsilon}))^2}{6} \tag{23}$$

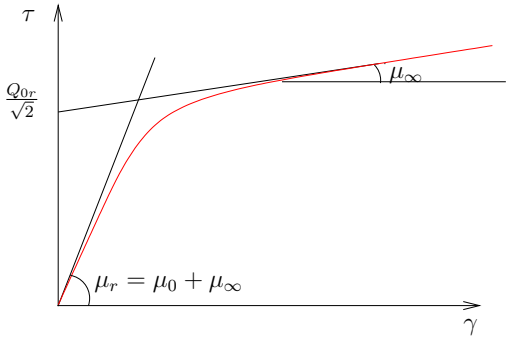

Figure 19: Material parameters involved in the hyperelastic law proposed by Favier et al. <69; 70> during a pure shear test.

To determine the influence of this behavioural law, numerical comparisons were performed on the displacement of the cushion and its stress distribution in the case of both this non linear evolution and an equivalent elastic law. The stress-strain curves obtained with both of these two laws are presented in fig. 20 and compared with those obtained a uniaxial tensile test performed in <71> at a strain-rate of $3.6\%/min$ on a film with the same thickness as that of which this cushion was made.

The material parameters involved in these two laws are presented in table 2. Contrary to the test on a cushion described in section 4.3, a pressure of 2 kPa was applied here to a square cushion 2000 mm in length and 0.25 mm thick. Due to the symmetry, only an eighth of the square was simulated.

These simulations were performed with a mesh consisting of 15×15 quadrangular elements, using linear interpolation methods. The value of parameter λ involved in the DR method was set at 3.

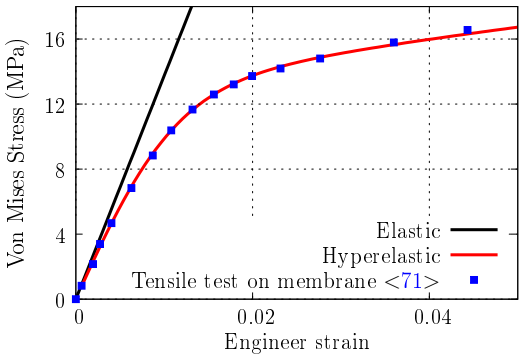

Figure 20: Comparison between the elastic and hyperelastic responses during a uniaxial tensile test presented in <71>.

Elastic parameters		Favier's Hyperelastic parameters			
E (MPa)	ν	K (MPa)	Q_{or} (MPa)	μ_r (MPa)	μ_∞ (MPa)
1375	0.4	3000	10.5	430	35

Table 2: Material parameters of the elastic and hyperelastic laws used to simulate the inflation of a cushion.

The global equilibria obtained with the two laws can be compared in Figure 21a. This figure gives the vertical displacement of the symmetrical horizontal line of the cushion at the end of the inflation. The shape of the cushion is almost identical with both the elastic and hyperelastic laws. The evolution of the major principal stress σ_{I} along the symmetrical horizontal line of the cushion is presented in fig. 21b. The non-linearity of the hyperelastic law results in a different pattern of stress distribution, especially in the centre of the cushion. However, it is worth noting that the location of

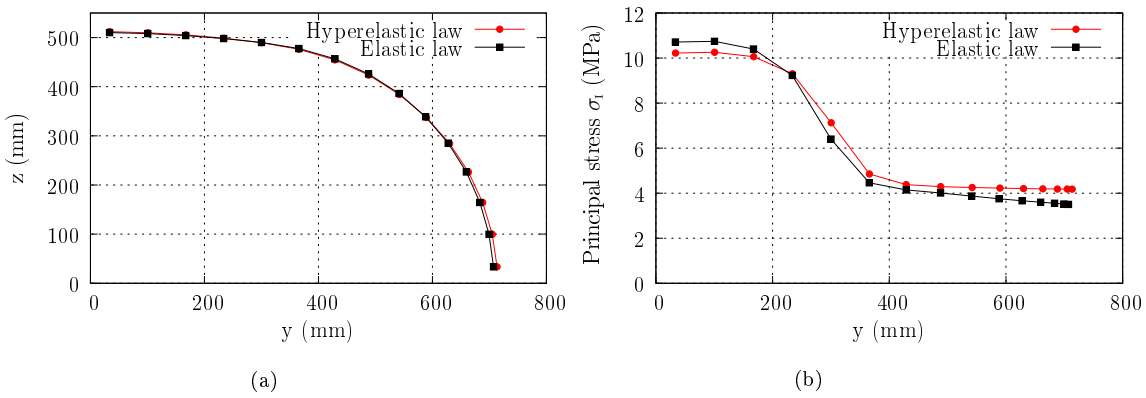

Figure 21: (a) Vertical displacement and (b) Evolution of the major principal stress σ_I along the symmetrical horizontal line of the cushion with elastic and hyperelastic laws.

the wrinkles is independent of the constitutive law used. Their location is similar to that previously observed in fig. 16a.

5. Application of the PS−DPS model: Zero Pressure Balloon inflation

In this section, the inflation of a Zero Pressure Balloon (ZPB) is simulated using the PS−DPS model both with an elastic law and with the same hyperelastic law as in the previous section.

During stratospheric missions, the volume of these balloons depends on their altitude (see fig. 22.a). These variations are caused by changes of temperature and pressure inside the balloons. At the start of the take-off and throughout these missions (see fig. 22.b), the wrinkles on the balloon continue to evolve. Accounting numerically for wrinkles in these structures is particularly important because the gas pressure, which depends on the volume of the balloon, affects the stress field. The DR method has often been used to simulate these inflation and wrinkle processes <40; 53–56>.

To test the validity the operation of the model and investigate the impact

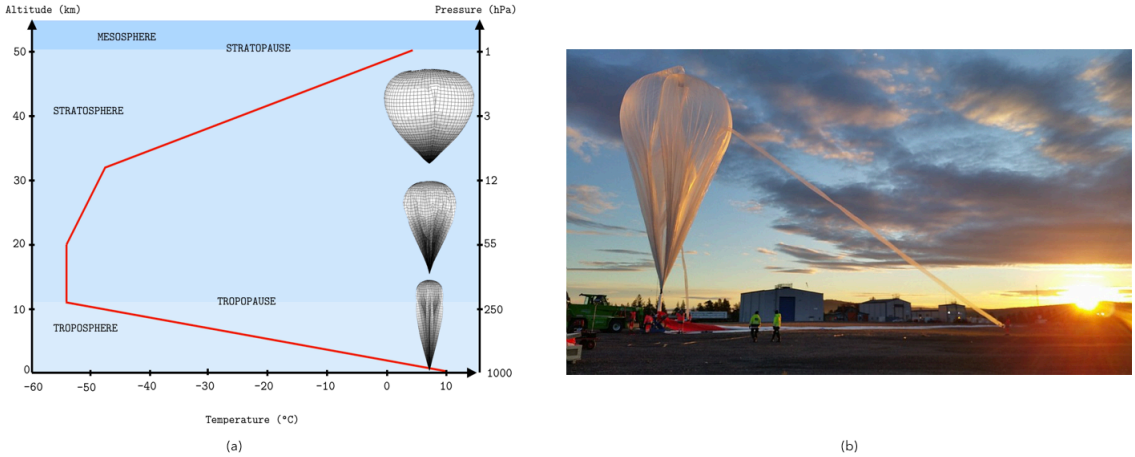

Figure 22: (a) Evolution of the pressure and temperature during a flight mission. (b) Photo of a ZPB before take-off <72>.

of wrinkles on a real structure, equilibrium configurations were calculated during all the phases of a ZPB flight (during take-off and flight, depending on the altitude and the internal pressure) using both elastic and hyperelastic laws. The numerical conditions used in the simulations are presented in fig. 23 and table 3.

The ZPB is composed of 74 gores, but only one gore of the balloon was simulated, and conditions of cyclic symmetry were imposed on the edges of the gore in order to account for this hypothesis. The gores, which are made of an LLDPE film, are assembled with polyester fiber reinforced tapes. In the case of these large-sized balloons, the main load to be simulated is the pressure gradient Δp in the balloon, which reflects the effects of the gas on the film. This gradient is calculated by subtracting the pressure in the balloon from the external pressure. It depends on the balloon's altitude z, which is an input parameter in the simulation and the thickness h of the film. The weight of the film and that of the tapes is accounted for in the simulations by a loading gravity condition. The mass of the pole piece (9.2 kg) is significant

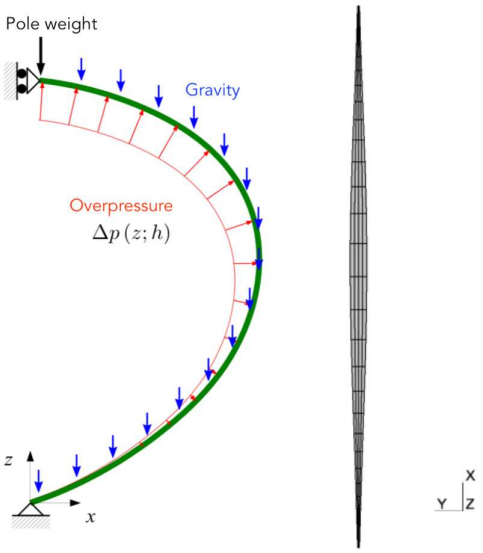

Figure 23: Mesh and loads applied during the ZPB simulations <73>.

Properties	Film	Tapes
Young's modulus (MPa)	1883	5986
Thickness h (μm)	25	-
Poisson's ratio	0.45	0.3
Density ρ (kg/m^3)	913	830

(a) Film's and tapes' elastic properties

Favier's hyperelastic parameters of the film			
K (MPa)	Q_{or} (MPa)	μ_r (MPa)	μ_∞ (MPa)
1000	18.95	614.17	0.6

(b) Hyperelastic parameters used to model the film

Table 3: Material properties of the film and tapes.

since it affects the shape of the balloon, and it is therefore simulated here in terms of its weight in the form of vertical point forces applied to the nodes at the end of the gore. These various loads and the mesh used are presented

in fig. 23. This mesh is composed of 120 quadrangular elements with linear interpolation, and 90 bar elements with linear interpolation stand for the assembly tapes. These tapes are located in the middle of the gore with an equivalent section of 9.586 mm^2. The contact between film and tapes is assumed to be perfect.

To simulate all the phases in the ZPB inflation process, two stages are defined:

1. The first stage consists in inflating the gore by applying the hydrostatic pressure gradually until the maximum altitude of 32.5 km is reached. During this phase, the boundary conditions for the hook and pole are applied but not the conditions of cyclic symmetry. The parameter λ in the DR method is set at 0.6. To speed up the calculation time, only the PS model is used at the start of the calculation. At the end of this step, the PS−DPS model is activated.

2. The second stage consists in applying the conditions of cyclic symmetry by means of linear boundary conditions. During this stage, the parameter λ is set at 2 and 12 with the elastic and hyperelastic law, respectively.

Comment 1. The initial configuration is the flat shape of the gore.

Comment 2. The parameter λ involved in the DR method is greatly increased in the case of the hyperelastic model because the non-linear part gives rise to many kinetic peaks at the end of the simulation.

Figure 24a shows the shape of the balloon with the PS and PS−DPS models in the case of elastic behaviour and with the PS−DPS model using the hyperelastic model. The overall shape of the gore differs slightly between the models tested because modelling a single gore of the balloon constrains

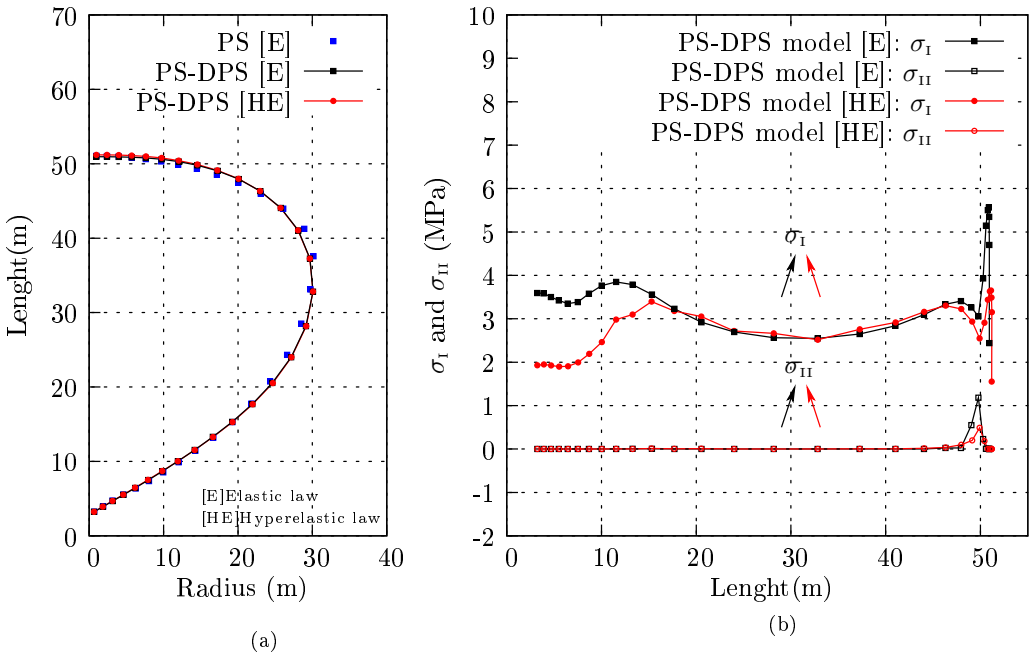

Figure 24: (a) Comparison on the ZPB shape between the PS and PS−DPS models, depending on the behavioural laws used. (b) Comparison on the local stress equilibrium in the ZPB between the elastic law [E] and the hyperelastic law [HE] with the PS−DPS model.

the shape of the final gore, which results in a slight difference in the overall shape depending on the type of law used. The major and minor principal stresses $\sigma_{\mathrm{I}max}$ and $\sigma_{\mathrm{II}min}$ in all the gores are presented in table 4. Contrary to the shape, the stress field differs considerably between the PS and PS−DPS models. During these simulations, the ZPB is not very heavily loaded mechanically. However, contrary to results obtained with the PS−DPS model, stress patterns obtained with the PS model are greatly disturbed by the presence of wrinkles on the balloon, which shows that taking these wrinkles into account greatly affects the simulations. The distribution of the major and minor principal stresses along the middle of the gore with the PS−DPS model are presented in fig. 24b. The stress levels obtained with the elastic

and hyperelastic laws are very low in these cases. However, the top and bottom of the balloon are the places where the films are the most heavily loaded, and where the influence of the constitutive law is the strongest.

	Elastic law		Hyperelastic law
	PS model	PS−DPS model	PS−DPS model
$\sigma_{\text{II}min}$ (MPa)	-1820.	0.	0.
$\sigma_{\text{I}max}$ (MPa)	115	5.56	3.65
Computation time for one iteration in the second stage (s/it)	0.150	0.542	1.097

Table 4: Major and minor principal stresses obtained in all the surface of the ZPB with the PS and PS−DPS models. Impact of the behavioural law used on the computational time in the case of a balloon.

The results of the stress fields presented in the table 4 and the figure 24*b* are in adequacy with the numerical results of the balloons of the same types <74; 75>. However, the materials, the number of balloon gores, the tapes assemblies used and the weight carried during a mission make comparisons between studies difficult.

Figure 25 shows the kinetic energy versus the iterations performed during the final stage in the calculations (pressure at the altitude targeted, activation of the wrinkling model in two cases). With the PS model, the evolution of the kinetic energy is very pronounced between each peak. Table 4 shows the time required by the two models to perform an iteration in this final stage. In the case of the PS model, this time was 0.15 s in the case of the elastic law, but 3.6 times longer in that of the PS−DPS model. However, contrary to the PS−DPS model, a larger number of iterations was necessary

to reach convergence with the PS model, but the time required was very short due to the simplicity of the elastic law used. When the balloon is inflated without using the wrinkling model, the local stress field is very noisy because of the presence of these wrinkles. Balancing these internal stresses can be detrimental to the convergence with the PS model, whereas the number of iterations required to reach convergence is much smaller with the PS−DPS model.

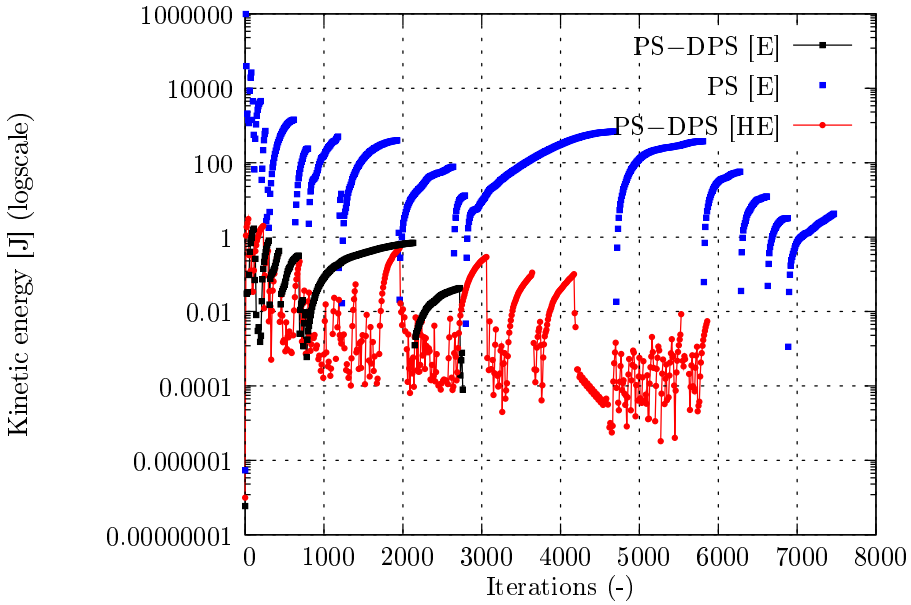

Figure 25: Evolution of the kinetic energy in the last step of the calculations in the case of the PS−DPS model with an elastic law and a hyperelastic law and that of the PS model with an elastic law.

The use of the non-linear hyperelastic law and the PS−DPS model yielded many peaks in the kinetic energy. The evolution of the kinetic energy between peaks was less visible than with the other models with a linear law. However, despite the increase observed in the λ factor (which increased by 6 fold in comparison with the elastic law), the simulation was still rather unstable. The calculation time required for each iteration was twice as long as with

the PS−DPS model with an elastic law. During this simulation, the kinetic damping used in the DR algorithm was found to slow down the convergence. In fact, a large number of kinetic energy peaks was always observed, especially at the end of the calculation. This somewhat chaotic nature of the kinetic damping may be increased by the non-linear law used to simulate the film. These results therefore show that the long computational times are mainly due to the complexity of the non-linear law used in this case, which also gives rise to convergence problems

These simulations point to the conclusion that the use of the PS−DPS and PS models is indicated on real-life structures. They show that the local stresses at work in the structure are more intense and differently distributed when complex behavioural laws are used in the simulations. In the context of stratospheric balloons, the use of a non-linear model resembling real-life behaviour more closely is essential to the successful design and development of these structures. The possibility of using a wrinkling model with more complex constitutive laws provides the most reliable means of predicting balloons' process of inflation during their missions.

6. Conclusion and outlook

A new wrinkling model named the PS-DPS model, which can be used with non-linear behaviour of all kinds is presented here. This model, based on the Almansi strain involves the use of a pseudo-Dynamic Relaxation method to determine the shape of flexible structures. Two plane stress conditions are imposed to simulate the wrinkled part in a state of uniaxial tension on the plane of the membrane. This model was first tested with a linear elastic behavioural law on numerical data in the literature in order to check its efficiency in classical cases. Lastly, the PS-DPS model was used to simulate the

inflation of a zero pressure balloon and found to be compatible with complex laws such as non-linear hyperelastic behavioural laws on real-life structures. A constitutive model of this kind was found to be the most suitable for describing the mechanical behaviour of the films of which stratospheric balloons are made.

Further studies on the PS-DPS model are also under way in order to improve its responses when used with incremental anisotropic laws. Another drawback observed when the pseudo-Dynamic Relaxation method was used with complex constitutive laws is that the time to convergence required to determine local equilibria is very long. In addition, with the wrinkling model, the computational time tends to be slightly longer than with a so-called conventional membrane model. It is therefore now proposed to develop new numerical strategy in future studies in order to reduce the computational time requirements of the model, especially when a complex behavioural law is used

CRediT author statement

H. Le Meitour: Validation, Investigation, Formal analysis, Writing - original draft. **G. Rio**: Conceptualization, Methodology, Investigation, Software, Writing - review & editing, Supervision. **H. Laurent**: Investigation, Writing - review & editing, Visualization, Resources, Funding acquisition, Supervision. **A. S. Lectez**: Data Curation, Resources, Writing - review & editing, Supervision. **P. Guigue**: Project administration, Funding acquisition, Supervision.

Acknowledgements

This research was supported by the CNES (team DSO/BL/VP), the company CNIM AIR SPACE and the Brittany Region (MITOFERM:0461/ARE11219/00030953) under contract N° 2840-2841/2017-00721. The authors would like to thank Julien Troufflard (a freelance engineer) and Frank Petitjean from the company RTIME for their useful suggestions and discussions.

Appendices

To clarify the following calculations of the tangent matrices, the following notations have been introduced: "3D" for the general 3D behaviour, "PS" for the specific 2D Plane Stress and "DPS" for the specific 1D Plane Stress when wrinkles occur.

A. Calculation of the tangent matrix in the PS model

When modelling the membrane, the plane stress condition has to be always satisfied, that is: $\sigma^{33}_{PS}(\varepsilon_{33}) = 0$. The differential therefore also has to be zero: $d\sigma^{33}_{PS}\ (\varepsilon_{33}) = 0$

Due to the method used to enforce the plane stress, the $\varepsilon_{33_{(t+\Delta t)}}$ obtained is in fact an implicit function of the in-plane deformations $\varepsilon_{\gamma\eta}$ where $\gamma, \eta =$ 1 and 2 and we can write:

$$0 = \frac{\partial \sigma^{33}}{\partial \varepsilon_{\gamma\eta}}(PS) = \frac{\partial \sigma^{33}}{\partial \varepsilon_{\gamma\eta}}(3D) + \frac{\partial \sigma^{33}}{\partial \varepsilon_{33}}(3D)\ \frac{\partial \varepsilon_{33}}{\partial \varepsilon_{\gamma\eta}}$$

which leads to the relations:

$$\frac{\partial \varepsilon_{33}}{\partial \varepsilon_{\gamma\eta}} = -\left[\frac{\partial \sigma^{33}}{\partial \varepsilon_{33}}(3D)\right]^{-1}\ \frac{\partial \sigma^{33}}{\partial \varepsilon_{\gamma\eta}}(3D)$$

which are used to obtain the tangent matrix (where $\alpha, \beta = 1$ and 2):

$$\frac{\partial \sigma^{\alpha\beta}}{\partial \varepsilon_{\gamma\eta}}(PS) = \frac{\partial \sigma^{\alpha\beta}}{\partial \varepsilon_{\gamma\eta}}(3D) + \frac{\partial \sigma^{\alpha\beta}}{\partial \varepsilon_{33}}(3D)\ \frac{\partial \varepsilon_{33}}{\partial \varepsilon_{\gamma\eta}}$$

B. Calculation of the tangent matrix in the PS-DPS model

The general expression for the tangent matrix is:

$$\frac{\partial \sigma^{ef}}{\partial \varepsilon_{kl}}(DPS) = \frac{\partial \sigma^{ef}}{\partial \varepsilon_{kl}}(3D) + \frac{\partial \sigma^{ef}}{\partial \varepsilon_{gh}}(3D)\ \frac{\partial \varepsilon_{gh}}{\partial \varepsilon_{kl}} \tag{24}$$

where $e, f = 2$ and 3. The degrees of freedom of the DPS condition in the present case are ε_{ee}, where $e = 2$ and 3. In this context, the relevant unknowns in relation (24) are the values of $\frac{\partial \varepsilon_{ee}}{\partial \varepsilon_{11}}$. We use the conditions $\sigma^{ee} = 0$ that must always be satisfied in DPS to calculate these values :

$$\frac{\partial \sigma^{ee}}{\partial \varepsilon_{11}}(DPS) = 0 = \frac{\partial \sigma^{ee}}{\partial \varepsilon_{11}}(3D) + \frac{\partial \sigma^{ee}}{\partial \varepsilon_{ff}}(3D)\ \frac{\partial \varepsilon_{ff}}{\partial \varepsilon_{11}}$$

and hence:

$$\frac{\partial \varepsilon_{ff}}{\partial \varepsilon_{11}} = -\left[\frac{\partial \sigma^{ee}}{\partial \varepsilon_{ff}}(3D)\right]^{-1}\ \frac{\partial \sigma^{ff}}{\partial \varepsilon_{11}}(3D)$$

The final tangent operator can then be calculated as follows:

$$\frac{\partial \sigma^{11}}{\partial \varepsilon_{11}}(DPS) = \frac{\partial \sigma^{11}}{\partial \varepsilon_{11}}(3D) + \frac{\partial \sigma^{11}}{\partial \varepsilon_{ff}}(3D)\ \frac{\partial \varepsilon_{ff}}{\partial \varepsilon_{11}}$$

References

[1] C. H. Jenkins, Nonlinear Dynamic Response of Membranes: State of the Art - Update, Appl. Mech. Rev 49 (10S) (1996) S41–S48. doi:10.1115/1.3101975.

[2] A. Adler, M. Mikulas, Application of a wrinkled membrane finite element approach to advanced membrane structures, American Institute of Aeronautics and Astronautics. (Aug. 2001). doi:10.2514/6.2001-4646.

[3] W. Wong, S. Pellegrino, Wrinkled membranes III: numerical simulations, Journal of Mechanics of Materials and Structures 1 (1) (2006) 63–95. doi:10.2140/jomms.2006.1.63.

[4] A. Jarasjarungkiat, R. Wüchner, K. U. Bletzinger, A wrinkling model based on material modification for isotropic and orthotropic membranes, Computer Methods in Applied Mechanics and Engineering 197 (6) (2008) 773–788. doi:10.1016/j.cma.2007.09.005.

[5] S. Kumar, S. H. Upadhyay, A. C. Mathur, Wrinkling Simulation of Membrane Structures under Tensile and Shear Loading, Journal of Vibration Analysis, Measurement, and Control 3 (1) (2015) 17. doi:10.7726/jvamc.2015.1002.

[6] X. F. Wang, Q. S. Yang, S.-s. Law, Wrinkled membrane element based on the wrinkling potential, International Journal of Solids and Structures 51 (21) (2014) 3532–3548. doi:10.1016/j.ijsolstr.2014.06.004.

[7] Y. Miyazaki, Wrinkle/slack model and finite element dynamics of membrane, International Journal for Numerical Methods in Engineering 66 (7) (2006) 1179–1209. doi:10.1002/nme.1588.

[8] X. Wang, S.-s. Law, Q. Yang, N. Yang, Numerical study on the dynamic properties of wrinkled membranes, International Journal of Solids and Structures 143 (2018) 125–143. doi:10.1016/j.ijsolstr.2018.03.001.

[9] X. Deng, Y. Xu, C. Clarke, Wrinkling modelling of space membranes subject to solar radiation pressure, Composites Part B: Engineering. (Aug. 2018). doi:10.1016/j.compositesb.2018.08.088.

[10] H. Wagner, Flat sheet metal girders with very thin metal web. Part I : : general theories and assumptions, National Advisory Committee for Aeronautics, 1931, oCLC: 919168471.
URL http://app.knovel.com/hotlink/toc/id:kpFSMGVT11/flat-sheet-metal

[11] E.-S. Lee, S.-K. Youn, Finite element analysis of wrinkling membrane structures with large deformations, Finite Elements in Analysis and Design 42 (8-9) (2006) 780–791. doi:10.1016/j.finel.2006.01.004.

[12] D. G. Roddeman, Finite-element analysis of wrinkling membranes, Communications in Applied Numerical Methods 7 (4) (1991) 299–307. doi:10.1002/cnm.1630070408.

[13] C. H. Wu, T. R. Canfield, Wrinkling in finite plane-stress theory, Quarterly of Applied Mathematics 39 (2) (1981) 179–199. doi:10.1090/qam/625468.

[14] A. C. Pipkin, The Relaxed Energy Density for Isotropic Elastic Membranes, IMA Journal of Applied Mathematics 36 (1) (1986) 85–99. doi:10.1093/imamat/36.1.85.

[15] E. M. Haseganu, D. J. Steigmann, Analysis of partly wrinkled membranes by the method of dynamic relaxation, Computational Mechanics 14 (6) (1994) 596–614. doi:10.1007/BF00350839.

[16] D. J. Steigmann, A. C. Pipkin, Finite deformations of wrinkled membranes, The Quarterly Journal of Mechanics and Applied Mathematics 42 (3) (1989) 427–440. doi:10.1093/qjmam/42.3.427.

[17] T. Raible, K. Tegeler, S. Löhnert, P. Wriggers, Development of a wrinkling algorithm for orthotropic membrane materials, Computer Methods in Applied Mechanics and Engineering 194 (21) (2005) 2550–2568. doi:10.1016/j.cma.2004.07.045.

[18] M. Epstein, M. A. Forcinito, Anisotropic membrane wrinkling: theory and analysis, International Journal of Solids and Structures 38 (30) (2001) 5253–5272. doi:10.1016/S0020-7683(00)00346-2.

[19] A. Jarasjarungkiat, R. Wüchner, K.-U. Bletzinger, Efficient sub-grid scale modeling of membrane wrinkling by a projection method, Computer Methods in Applied Mechanics and Engineering 198 (9-12) (2009) 1097–1116. doi:10.1016/j.cma.2008.11.014.

[20] S. Kang, S. Im, Finite Element Analysis of Wrinkling Membranes, Journal of Applied Mechanics 64 (2) (1997) 263. doi:10.1115/1.2787302.

[21] X. Liu, C. H. Jenkins, W. W. Schur, Large deflection analysis of pneumatic envelopes using a penalty parameter modified material model, Finite Elements in Analysis and Design 37 (3) (2001) 233–251. doi:10.1016/S0168-874X(00)00040-8.

[22] K. Woo, H. Igawa, C. H. Jenkins, Analysis of Wrinkling Behavior of

Anisotropic Membrane, CMES: Computer Modeling in Engineering & Sciences 6 (4) (2004) 397–408. doi:10.3970/cmes.2004.006.397.

[23] R. K. Miller, J. M. Hedgepeth, An algorithm for finite element analysis of partly wrinkled membranes, AIAA Journal 20 (12) (1982) 1761–1763. doi:10.2514/3.8018.

[24] R. K. Miller, J. M. Hedgepeth, V. I. Weingarten, P. Das, S. Kahyai, Finite element analysis of partly wrinkled membranes, Computers & Structures 20 (1) (1985) 631–639. doi:10.1016/0045-7949(85)90111-7.

[25] A. Adler, M. Mikulas, J. Hedgepeth, Static and dynamic analysis of partially wrinkled membrane structures, in: 41st Structures, Structural Dynamics, and Materials Conference and Exhibit, American Institute of Aeronautics and Astronautics, Atlanta,GA,U.S.A., 2000. doi:10.2514/6.2000-1810.

[26] H. Ding, B. Yang, The modeling and numerical analysis of wrinkled membranes, International Journal for Numerical Methods in Engineering 58 (12) (2003) 1785–1801. doi:10.1002/nme.832.

[27] T. Akita, K. Nakashino, M. C. Natori, K. C. Park, A simple computer implementation of membrane wrinkle behaviour via a projection technique, International Journal for Numerical Methods in Engineering 71 (10) (2007) 1231–1259. doi:10.1002/nme.1990.

[28] L. Zheng, Wrinkling of dielectric elastomer membranes, Ph.D. thesis, California Institute of Technology, Pasadena, CA. (2009).
URL http://resolver.caltech.edu/CaltechETD:etd-09222008-161217

[29] E. Oñate, F. Zárate, Rotation-free triangular plate and shell elements, International Journal for Numerical Methods in Engineering 47 (1-3) (2000) 557–603. doi:10.1002/(SICI)1097-0207(20000110/30)47:1/3<557::AID-NME784>3.0.CO;2-9.

[30] H. Laurent, G. Rio, Formulation of a thin shell finite element with continuity C^0 and convected material frame notion, Computational Mechanics 27 (3) (2001) 218–232. doi:10.1007/s004660100243.

[31] F. G. Flores, E. Oñate, Improvements in the membrane behaviour of the three node rotation-free BST shell triangle using an assumed strain approach, Computer Methods in Applied Mechanics and Engineering 194 (6) (2005) 907–932. doi:10.1016/j.cma.2003.08.012.

[32] Y. Lecieux, R. Bouzidi, Experimental analysis on membrane wrinkling under biaxial load - Comparison with bifurcation analysis, International Journal of Solids and Structures 47 (18) (2010) 2459–2475. doi:10.1016/j.ijsolstr.2010.05.005.

[33] F. G. Flores, E. Oñate, Wrinkling and folding analysis of elastic membranes using an enhanced rotation-free thin shell triangular element, Finite Elements in Analysis and Design 47 (9) (2011) 982–990. doi:10.1016/j.finel.2011.03.014.

[34] T. Iwasa, Approximate estimation of wrinkle wavelength and maximum amplitude using a tension-field solution, International Journal of Solids and Structures 121 (2017) 201 – 211. doi:10.1016/j.ijsolstr.2017.05.029.

[35] P. Contri, B. A. Schrefler, A geometrically nonlinear finite element analysis of wrinkled membrane surfaces by a no-compression material

model, Communications in Applied Numerical Methods 4 (1) (1988) 5–15. doi:10.1002/cnm.1630040103.

[36] T. Gerngross, S. Pellegrino, Anisotropic Viscoelasticity and Wrinkling of Superpressure Balloons: Simulation and Experimental Verification, in: AIAA Balloon Systems Conference, BLN-6: Materials and Structures II, 2009. doi:10.2514/6.2009-2815.

[37] T. Gerngross, Y. Xu, S. Pellegrino, Viscoelastic behaviour of pumpkin balloons, Advances in Space Research 42 (10) (2008) 1683–1690. doi:10.1016/j.asr.2007.03.093.

[38] X. Deng, S. Pellegrino, Wrinkling of orthotropic viscoelastic membranes, AIAA Journal 50 (3) (2012) 668–681. doi:10.2514/1.J051255.

[39] K. Kwok, S. Pellegrino, Large strain viscoelastic model for balloon film, in: AIAA (Ed.), 11th AIAA Aviation Technology, Integration, and Operations (ATIO) Conference, American Institute of Aeronautics and Astronautics, 2011. doi:10.2514/6.2011-6939.

[40] D. Wakefield, A. Bown, Non-Linear Analysis of the NASA Super Pressure Balloons: Some Detailed Investigations of Recent Antarctic Flight Balloons, in: 11th AIAA Aviation Technology, Integration, and Operations (ATIO) Conference, American Institute of Aeronautics and Astronautics, 2011. doi:10.2514/6.2011-6829.

[41] V. Nayyar, K. Ravi-Chandar, R. Huang, Stretch-induced stress patterns and wrinkles in hyperelastic thin sheets, International Journal of Solids and Structures 48 (25) (2011) 3471–3483. doi:10.1016/j.ijsolstr.2011.09.004.

[42] C. Fu, T. Wang, F. Xu, Y. Huo, M. Potier-Ferry, A modeling and resolution framework for wrinkling in hyperelastic sheets at finite membrane strain, Journal of the Mechanics and Physics of Solids 124 (2019) 446–470. doi:10.1016/j.jmps.2018.11.005.

[43] R. Ziegler, W. Wagner, K.-U. Bletzinger, A Finite Element Model for the Analysis of Wrinkled Membrane Structures, International Journal of Space Structures 18 (1) (2003) 1–14. doi:10.1260/026635103769016591.

[44] M. R. Barnes, Form Finding and Analysis of Tension Structures by Dynamic Relaxation, International Journal of Space Structures 14 (2) (1999) 89–104. doi:10.1260/0266351991494722.

[45] P. Underwood, Dynamic Relaxation, in Computational methods for transient analysis. Eds T. Belytschko, T. J.R. Hugues. Elsevier Science Publishers Amsterdam : North-Holland., 1983, Ch. 5, pp. 245–265. doi:10.1002/zamm.19860660905.

[46] G. Rio (Ed.), Herezh++: FEM software for large transformations in solids, Université de Bretagne Sud, dépôt APP (Agence pour la Protection des Programmes) - Certification IDDN-FR-010-0106078-000-R-P-2006-035-20600, 2006.

[47] H. Laurent, G. Rio, A. Vandenbroucke, N. Aït Hocine, Experimental and numerical study on the temperature-dependent behavior of a fluoroelastomer, Mechanics of Time-Dependent Materials 18 (4) (2014) 721–742. doi:10.1007/s11043-014-9247-3.

[48] J. Troufflard, H. Laurent, G. Rio, B. Omnès, S. Javanaud, Temperature-dependent modelling of a HNBR O-ring seal above and below the glass

transition temperature, Materials & Design 156 (2018) 1–15. doi:10.1016/j.matdes.2018.06.016.

[49] Abaqus, ABAQUS/Standard User's Manual, Version 6.14 (2014).

[50] P. Y. Manach, G. Rio, Analysis of orthotropic behavior in convected coordinate frames, Computational Mechanics 23 (5) (1999) 510–518. doi:10.1007/s004660050430.

[51] D. G. Roddeman, J. Drukker, C. W. J. Oomens, J. D. Janssen, The Wrinkling of Thin Membranes: Part I—Theory, J. Appl. Mech 54 (4) (1987) 884–887. doi:10.1115/1.3173133.

[52] J. Troufflard, Étude numérique et expérimentale des structures gonflables : applications aux gilets de sauvetage gonflables, Phd thesis, Lorient (Jan. 2011).
URL http://www.theses.fr/2011LORIS223

[53] D. Wakefield, Numerical Modelling of Pumpkin Balloon Instability, in: AIAA 5th ATIO and16th Lighter-Than-Air Sys Tech. and Balloon Systems Conferences, American Institute of Aeronautics and Astronautics, 2005. doi:10.2514/6.2005-7445.

[54] D. Wakefield, Numerical Investigations of Pumpkin Balloon Deployment Stability, in: AIAA Balloon Systems Conference, American Institute of Aeronautics and Astronautics, 2007. doi:10.2514/6.2007-2604.

[55] D. Wakefield, Non-Linear Viscoelastic Analysis and the Design of Super Pressure Balloons: Stress, Strain and Stability, in: AIAA Balloon Systems Conference, American Institute of Aeronautics and Astronautics, 2009. doi:10.2514/6.2009-2813.

[56] D. Wakefield, A. Bown, Non-Linear Analysis of the NASA Super Pressure Balloons: Whole Flight Simulations, in: AIAA Balloon Systems Conference, American Institute of Aeronautics and Astronautics, 2017. doi:10.2514/6.2017-3606.

[57] J. R. Garcia, Numerical study of dynamic relaxation methods and contribution to the modelling of inflatable lifejackets, Phd thesis, Université de Bretagne Sud (Dec. 2011).
URL https://tel.archives-ouvertes.fr/tel-00659669/document

[58] J. Rodriguez, G. Rio, J. M. Cadou, J. Troufflard, Numerical study of dynamic relaxation with kinetic damping applied to inflatable fabric structures with extensions for 3d solid element and non-linear behavior, Thin-Walled Structures 49 (11) (2011) 1468–1474. doi:10.1016/j.tws.2011.07.011.

[59] R. Courant, K. Friedrichs, H. Lewy, On the Partial Difference Equations of Mathematical Physics, IBM Journal of Research and Development 11 (2) (1967) 215–234. doi:10.1147/rd.112.0215.

[60] Mansfield Eric Harold, Pugsley Alfred Grenville, Load transfer via a wrinkled membrane, Proceedings of the Royal Society of London. A. Mathematical and Physical Sciences 316 (1525) (1970) 269–289. doi:10.1098/rspa.1970.0079.

[61] J. Leifer, W. Belvin, Prediction of Wrinkle Amplitudes in Thin Film Membranes Using Finite Element Modeling, in: 44th AIAA/ASME/ASCE/AHS/ASC Structures, Structural Dynamics, and Materials Conference, Structures, Structural Dynamics, and Materials

and Co-located Conferences, American Institute of Aeronautics and Astronautics, 2003. doi:10.2514/6.2003-1983.

[62] W. Wong, S. Pellegrino, Wrinkled membranes I: experiments, Journal of Mechanics of Materials and Structures 1 (1) (2006) 3–25. doi:10.2140/jomms.2006.1.3.

[63] W. Wong, S. Pellegrino, Wrinkled membranes II: analytical models., Journal of Mechanics of Materials and Structures 1 (1) (2006) 27–61. doi:10.2140/jomms.2006.1.27.

[64] M. M. Mikulas, Behavior of a flat stretched membrane wrinkled by the rotation of an attached hub, no. 30 p. in NASA TN D-2456, National Aeronautics and Space Administration. Langley Research Center, Washington, D.C., 1964.
URL //catalog.hathitrust.org/Record/011433642

[65] K. Lu, M. Accorsi, J. Leonard, Finite element analysis of membrane wrinkling, International Journal for Numerical Methods in Engineering 50 (5) (2001) 1017–1038. doi:10.1002/1097-0207(20010220)50:5<1017::AID-NME47>3.0.CO;2-2.

[66] E. Reissner, On Tension Field Theory, in: Fifth International Congress on Applied Mechanics, 1938, pp. 88–92.
URL https://books.google.fr/books?id=LUrNXwAACAAJ

[67] M. Stein, J. M. Hedgepeth, Analysis of partly wrinkled membranes, Washington, D.C. : National Aeronautics and Space Administration : [For sale by the Office of Technical Services, Dept. of Commerce], 1961.
URL https://trove.nla.gov.au/version/179471700

[68] X. Wang, J. Ma, S.-s. Law, Q. Yang, Numerical analysis of wrinkle-influencing factors of thin membranes, International Journal of Solids and Structures 97-98 (2016) 458–474. doi:10.1016/j.ijsolstr.2016.07.004.

[69] D. Favier, P. Guélin, P. Pegon, Thermomechanics of Hysteresis Effects in Shape Memory Alloys, MSF 56-58 (1991) 559–564. doi:10.4028/www.scientific.net/MSF.56-58.559.

[70] M. Zrida, H. Laurent, G. Rio, S. Pimbert, V. Grolleau, N. Masmoudi, C. Bradai, Experimental and numerical study of polypropylene behavior using an hyper-visco-hysteresis constitutive law, Computational Materials Science 45 (2) (2009) 516 – 527. doi:10.1016/j.commatsci.2008.11.017.

[71] C. Galliot, R. H. Luchsinger, Uniaxial and biaxial mechanical properties of ETFE foils, Polymer Testing 30 (4) (2011) 356–365. doi:10.1016/j.polymertesting.2011.02.004.

[72] CNES, last accessed May 2020. [link].
URL https://phototheque.cnes.fr

[73] F. Petitjean, G. Rio, A. Hamdani, X. Soors, Simulation du comportement de ballons stratosphériques ouverts, in: CSMA 2015 - 12ème Colloque National en Calcul des Structures, Giens, France, 2015.
URL https://hal.archives-ouvertes.fr/hal-01502302/file/csma2015_FP_GR.pdf

[74] W. W. Schur, J. M. Simpson, Finite element solution for the structural behavior of a scientific balloon, Advances in Space Research 13 (2) (1993) 45–48. doi:10.1016/0273-1177(93)90273-E.

URL http://www.sciencedirect.com/science/article/pii/027311779390273E

[75] W. W. Schur, Structural response of a zero-pressure balloon with an axial load tendon, in: International Balloon Technology Conference, Balloon Systems Conferences, American Institute of Aeronautics and Astronautics, 1997. doi:10.2514/6.1997-1475.
URL https://arc.aiaa.org/doi/10.2514/6.1997-1475